

Enhancing Coherence with a Clock Transition and Dynamical Decoupling in the Cr₇Mn Molecular Nanomagnet

Guanchu Chen,^{1,2} Brendan C. Sheehan,^{1,2,*} Ilija Nikolov,^{1,†} James W. Logan,^{1,*} Charles A. Collett,^{1,‡} Gajadhar Joshi,^{1,§} Grigore A. Timco,³ Jillian E. Denhardt,^{4,¶} Kevin R. Kittilstved,^{4,**} Richard E. P. Winpenny,³ and Jonathan R. Friedman^{1,2,††}

¹*Department of Physics and Astronomy, Amherst College, Amherst, MA 01002, USA*

²*Department of Physics, University of Massachusetts Amherst, Amherst, MA 01003, USA*

³*Department of Chemistry, The University of Manchester, Manchester M13 9PL, UK*

⁴*Department of Chemistry, University of Massachusetts, Amherst, MA 01003, USA*

(Dated: July 18, 2025)

Molecular magnets are attractive as spin qubits due to their chemical tunability, addressability through electron-spin resonance techniques, and long coherence times. Clock transitions (CTs), for which the system is immune to the effect of magnetic-field fluctuations to first order, provide a method to enhance the coherence time T_2 , and to reveal mechanisms of decoherence that are not due to such fluctuations. Here we investigate two variants of Cr₇Mn, a spin-1 molecular nanomagnet, at fields near a zero-field CT. We find that at temperatures ≤ 2 K, $T_2 \sim 1 \mu\text{s}$ at the CT using a Hahn-echo pulse sequence. Away from the CT, electron-spin-echo envelope modulation (ESEEM) oscillations due to coupling to nuclear spins are observed and have a T_2 as high as $1.35 \mu\text{s}$, indicating a distinct mechanism of coherence preservation. Dynamical decoupling with the CPMG pulse sequence yields $T_2 \sim 2.8 \mu\text{s}$ at the CT and up to $\sim 3.6 \mu\text{s}$ in the ESEEM regime along with a demodulation of the oscillatory behavior. The experimental values of T_2 are largely independent of the degree of dilution of the molecules in solvent or whether the solvent is deuterated, indicating that much of the decoherence and ESEEM arises from sources within the molecules themselves. To account for decoherence, we develop a model that includes not only field fluctuations but also fluctuations in the CT transition frequency itself. Our results can be well explained by treating the environment as a combination of noise at the nuclear Larmor precession frequency and $1/f$ noise in the transverse anisotropy parameter E . Such information about the microscopic origins of decoherence can aid the rational design of molecular-based spin qubits.

I. INTRODUCTION

At the core of quantum information science is the ability to manipulate a qubit – a two-level system that can exist in superposition of states for a nontrivial duration of time. Many physical systems have exhibited characteristics that make them attractive as qubits, including superconducting circuits [1], trapped ions [2], and spin qubits [3–8]. Molecular nanomagnets (MNM), paramagnetic molecules with a ground-state magnetic moment, are particularly interesting as spin qubits due to their chemically engineerable electronic spin states, which can be probed through the use of electron spin resonance (ESR) techniques [9–13]. To be considered a viable qubit,

an MNM must retain phase memory for times long compared to quantum gate operation times.

One way to achieve a long phase-memory (coherence) time T_2 is through a so-called clock transition (CT), which occurs at an avoided level crossing where the transition frequency ϵ between states is immune to the decohering effects of environmental noise to first order. CTs are commonly used in superconducting qubits, particularly the transmon and fluxonium, to provide isolation from fluctuations from charge and/or magnetic noise sources [14–18]. In spin systems, where decoherence is primarily due to magnetic-field fluctuations from environmental spins, a CT occurs when $\nabla_{\mathbf{B}}\epsilon = \mathbf{0}$; when this condition is fulfilled, T_2 is typically significantly enhanced. CTs have been observed in several spins systems, such as in Bi-doped silicon [19], the HoW₁₀ molecular magnet [20] and other MNMs [21–28], as well as spin defects in silica glasses [29]. In addition, theoretical work has proposed implementations of one- and two-qubit gates in an MNM dimer in which all of the relevant radiative transitions are CTs [30]. MNMs provide excellent testbeds for studying spin CTs because their properties can be chemical engineered. The local molecular environment can be adjusted via ligand-field tuning, isotopic purification, or choice of matrix (e.g. solvent), allowing control of the dominant decoherence channel for the system [31–34].

While CTs typically enhance T_2 , portending better

* Current address: Department of Physics and Astronomy, Dartmouth College, Hanover, NH 03755, USA

† Current address: Department of Physics, Brown University, Providence, RI 02912, USA

‡ Current address: Department of Physics, Hamilton College, Clinton, NY 13323, USA

§ Current address: Center for Integrated Nanotechnologies, Sandia National Laboratories, Albuquerque, NM 87123, USA

¶ Current address: University of Hawai'i at Mānoa, Honolulu, HI 96822, USA

** Current address: Department of Chemistry, Washington State University, Pullman, 99164-4630, USA

†† jrfriedman@amherst.edu

qubit performance, they also provide a window into the underlying decoherence mechanisms in a system. Since at a CT decoherence from magnetic-field fluctuations is suppressed, the remaining decoherence may arise from other sources, e.g. vibrations [35–37], that are not filtered by the CT. When one tunes away from the CT by changing the applied field, the system is more susceptible to decoherence from fluctuating fields and the change in coherence reflects the nature of these fluctuations. Gaining understanding about the sources of decoherence in spin qubits can thus provide fundamental information and aid in the rational design of the next generation of qubits.

In this work, we employ pulse ESR to study decoherence in the Cr_7Mn MNM near its zero-field CT [21]. We find T_2 values on the order of a few μs at the CT as well as in a range of fields where electron-spin-echo envelope modulation (ESEEM) oscillations are observed. Dynamical decoupling techniques provide further enhancement to coherence in both of these regimes. Through a combination of experimental studies and detailed modeling of the dependence of decoherence on field and pulse-sequence properties, we extract information about the environmental sources of noise that give rise to decoherence in this system. We find that the noise consists of field fluctuations arising from a nuclear spin bath combined with noise in the CT transition frequency itself. While the CT can effectively filter out magnetic field noise, it cannot filter the latter form of noise. This suggests that fluctuations in the CT frequency, arising from fluctuations in non-magnetic Hamiltonian parameters, may ultimately limit the efficacy of CTs in enhancing coherence.

Cr_7Mn is one of a group of heterometallic rings described by $\text{A}[\text{Cr}_7\text{MnF}_8\text{X}_{16}]$, where A is the cation and X indicates the ligand – in our samples, $\text{X} = (\text{CH}_3)_3\text{CCOO}^-$. In this work, we study two variants of Cr_7Mn that differ only in terms of cation: $\text{A} = (\text{CH}_3)_2\text{NH}_2^+$ (**1**) and $\text{A} = \text{Cs}^+$ (**2**) [34, 38]. The structure of **1** is shown in the inset of Fig. 1. These systems, and the structurally similar spin-1/2 Cr_7Ni , were previously reported to have T_2 ranging from a few hundred ns up to 15 μs at temperatures below 5 K in X-band [34, 39, 40]. While there has been much research on Cr_7Ni , [34, 40–45], which has $S = \frac{1}{2}$, Kramers’ theorem prohibits it from exhibiting a zero-field CT. In contrast, Cr_7Mn has a ground-state spin of $S = 1$ [38, 41, 46], the integer spin giving rise to a zero-field CT.

Typically spin CTs arise from one of two mechanisms: 1) Strong hyperfine coupling between an electronic and nuclear spin [22, 47, 48] or 2) Magnetic anisotropy with a significant transverse component. The latter mechanism is at play in Cr_7Mn , which at low temperature can be described by the spin Hamiltonian

$$\mathcal{H} = -DS_z^2 + E(S_x^2 - S_y^2) + g_s\mu_B\mathbf{B} \cdot \mathbf{S}, \quad (1)$$

where D and E are longitudinal and transverse anisotropy parameters, respectively. Previous work found the values of the anisotropy parameters to be $D = 21$ GHz, $E = 1.9$ GHz, and the Landé factor to

be $g = 1.96$ [21, 42], although there is substantial inhomogeneity in E , as discussed in more detail below. Working in the $\{|-1\rangle, |0\rangle, |1\rangle\}$ basis, the eigenbasis of S_z , the zero-field eigenstates of Eq. 1 are $|\pm\rangle = \frac{1}{\sqrt{2}}(|1\rangle \pm |-1\rangle)$ and $|0\rangle$ with energies $-D \pm E$ and 0, respectively. Because $D \gg E$ and given the probe frequencies used in our experiments, the $|0\rangle$ state can be ignored, resulting in an effective two-level system consisting of the states $|\pm\rangle$. At zero magnetic field, an avoided crossing with tunnel splitting energy $\epsilon = 2E$ emerges; when a magnetic field is applied to the two-level qubit, the energy levels exhibit a weak field dependence. Fig. 1(a) shows the level energies calculated as a function of field with the field oriented along the cardinal directions. As can be seen, an avoided crossing is present at zero field in this system regardless of the direction of the field. In other words, this system has the structure of a CT in which the transition frequency is independent of magnetic field to first order: $\nabla_{\mathbf{B}}\epsilon|_{B=0} = \mathbf{0}$. The system therefore experiences substantial protection from the decohering effects of magnetic-field fluctuations, leading to an enhancement of quantum coherence and the magnitude of the dephasing time T_2 .

At zero field, the transition between the $|\pm\rangle$ states is determined only by the anisotropy parameter E . However, we find a significant range of frequencies at which a zero-field transition is observed (see [49]), indicating a substantial inhomogeneity in the value of E . The effect of this inhomogeneity is schematically illustrated in Fig. 1(b), where we assume the value of E belongs to a Gaussian distribution. The figure shows the simulated transition frequencies as a function of the field oriented along the z direction, with color indicating the population of molecules in the ensemble with a specific transition frequency at a given applied field. Each solid gray line represents a different example of the transition frequency as a function of magnetic field for a single E value; the gray line with the lowest minimum at zero field has the smallest E . The dashed horizontal line illustrates how a single ESR frequency (of 5 GHz) samples a wide range of transition fields and therefore a wide range of E values. All of our experiments employ orientationally disordered samples, resulting in the probing of molecules with field components along the x and y directions. Since the transition frequency dependence is weaker for these directions (see Fig. 1(a)) than for z , the resulting broadening of the resonance in field is even wider than illustrated in Fig. 1(b).

II. METHODS

Samples were synthesized using procedures published previously [39]. In order to reduce the effects on intermolecular dipole interactions, we studied dilute samples using either solid or liquid solutions. For solid-solution samples, we co-crystallized Cr_7Mn with a diamagnetic isostructural analog, Ga_7Zn [21, 50]. Liquid

samples were made by dissolving the molecule in toluene and sealing the solution in a fused-silica capillary with a torch. For some samples, deuterated toluene was used as a solvent to mitigate potential decoherence from inter-

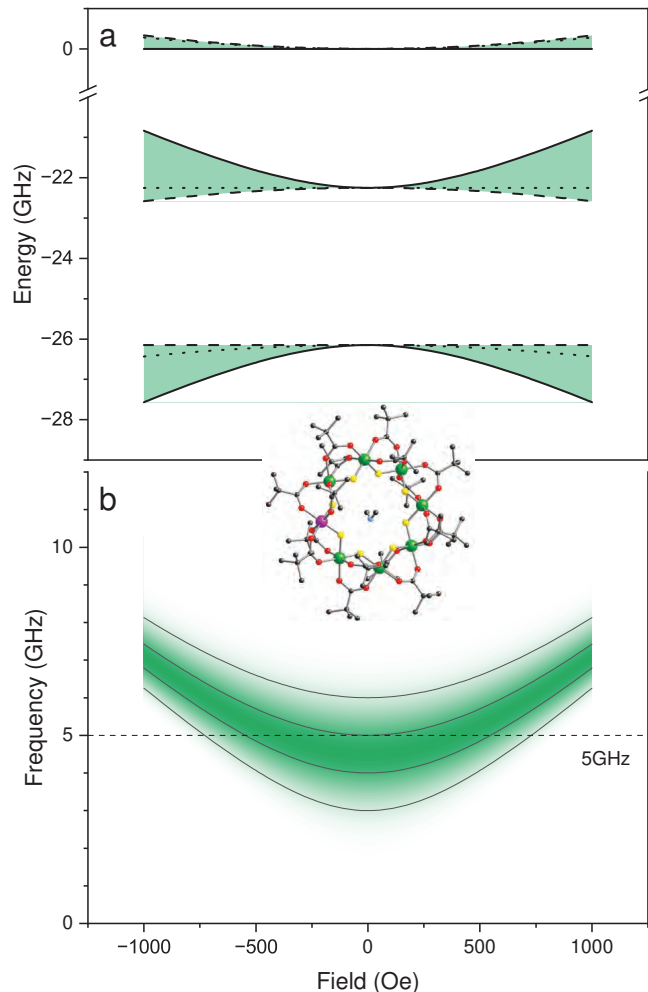


FIG. 1. Avoided crossing at zero field with broadening. a) Eigenenergies of the two lowest levels of Cr_7Mn , calculated from Eq. 1, as a function of field; solid, dashed, and dotted lines shows when the field is applied along the z , x , and y axes, respectively. The colored areas illustrate the range of energies given all possible orientations of field. b) Transition frequency as a function of magnetic field calculated from Eq. 1 and assuming that the field is directed along the easy (z) axis. To illustrate the effect of inhomogeneous broadening, we let the transverse anisotropy parameter E have a Gaussian distribution centered at $E = 2.25$ GHz with a full width at half maximum of 1 GHz. Color indicates probability density associated with this distribution at each field. The dashed line indicates an example probe frequency of 5 GHz, illustrating that, because of the significant broadening in this system, resonance with a single radiation frequency occurs over a wide range of magnetic fields. Inset shows a ball-and-stick diagram of **1**. Colors: Cr^{3+} (green), Mn^{2+} (purple), F (yellow), O (red), C (black), N (light blue). Hydrogens have been omitted for clarity.

actions with solvent protons. Dilution percentages indicated herein indicate volume fraction of Cr_7Mn molecules in solvent/matrix. We employed two different procedures to cool down the toluene-based samples: they were either gradually cooled down to the base temperature (~ 1.8 K) in a Quantum Design Physical Property Measurement System (PPMS) cryostat, or flash frozen in liquid nitrogen prior to being quickly inserted into a pre-cooled cryostat to prevent any thawing.

Despite using different cations, different host matrices, and different cooling techniques, all of our samples behave similarly across a broad frequency range (see [49] for comparisons). This suggests that the mechanisms of decoherence underlying our observations are rather distinct from what was investigated previously [34, 40], where ESR was performed at X-band at fields far from any CT.

ESR experiments were performed with the sample placed in a copper loop-gap resonator (LGR) [51] in a custom-designed probe with *in situ* frequency- and coupling-tuning capability [52]. To maximize signal from the CT, all data was collected using parallel mode ESR: the LGR's B_1 field was parallel to the DC field B_0 . CW reflection spectroscopy was performed via a direct-detection method (i.e. no field modulation) by monitoring the LGR's resonance with a Keysight E5063A vector network analyzer; as the field was swept, a change in the quality factor of the total resonance provided a measure of sample response. For pulsed spectroscopy we employed a homodyne detection scheme wherein a Tabor Electronics SE5082 arbitrary waveform generator (AWG), placed in a circuit with commercially available microwave electronics components, was used to generate pulses. Spin echoes were amplified, downconverted with a mixer, and then recorded with a digital oscilloscope. Phase cycling was used for background subtraction. A typical LGR used in this study has $Q \sim 2000$ at ~ 1.8 K; for pulsed measurements we placed Eccosorb-brand microwave absorber inside the copper shield near the resonator to lower the Q and preserve pulse-shape fidelity.

III. RESULTS

A typical CW spectrum of Cr_7Mn is shown in black in Fig. 2, taken of a 5% dilution solid solution of **1**. The spectrum shows a broad spectral peak with a width of ~ 4000 Oe. The large width suggests an inhomogeneous broadening of ~ 1 GHz in the transverse anisotropy parameter E , indicating a “softness” to the structure of the molecule, perhaps due to a distortion of the ring. A hole-burning experiment indicates that despite the significant broadening in our samples, for given frequency and field, we are addressing a small sub-ensemble of the sample (details in [49]).

Also shown in Fig. 2 is an electron spin echo (ESE) spectra (red), which has signal over a much narrower range of fields than the CW spectrum: despite a CW signal at fields up to ~ 4000 Oe, the echo signal is limited

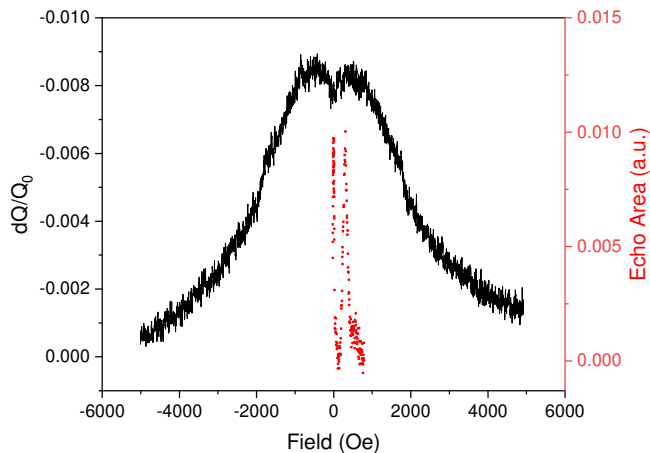


FIG. 2. Spectra obtained from Cr_7Mn . Black shows the continuous-wave spectrum taken on a sample of 5% dilution solid solution of **1** at 1.8 K, using a radiation frequency of 5.013 GHz. The fact that ESR signal is obtained over a rather wide range of field indicates the substantial inhomogeneous broadening in this system. Red shows the results of an echo-detected field spectrum on the same sample performed at 5.011 GHz and at 1.8 K using a pulse delay of $\tau = 800$ ns.

to fields below 1000 Oe. This suggests that for most fields away from zero field, the coherence time T_2 is too short to allow for an echo to be observed.

Fig. 3 shows echo-detected field-swept (EDFS) spectra from 1% dilution of **2** in toluene (black) or deuterated toluene (red) measured at 1.8 K at similar frequencies. The spectra were obtained with a Hahn sequence with a delay time of $\tau = 600$ ns. Two ESE peaks are visible; a narrow peak at zero field and a broad peak at higher field (in this case, ~ 390 Oe). The narrow peak at zero field we attribute to a CT [21]. The broader peak is the effect of ESEEM due to interactions with nuclear spins, as will be discussed in more detail below. Notably, we see very little difference between these two spectra, suggesting a limited role played by the solvent protons in producing the ESEEM behavior. We note the change in the amplitude of the ESEEM peak relative to the CT peak in Fig. 3 compared to Fig. 2, which is due to the different values of τ used to acquire the data in each figure.

Focusing on the CT peak, Fig. 4(a) shows the EDFS spectrum (red) overlaid with the coherence time T_2 (black) extracted from Hahn-echo data with a 5% dilution sample of **2**. Each T_2 value was extracted by varying the delay time τ in the Hahn sequence (Fig. 4(a) inset) and fitting the resulting decay to an exponential decay. The comparison in Fig. 4(a) shows that echo signal size and T_2 have similar behavior with field, indicating that the loss of echo signal with increasing field can be attributed to the reduction in T_2 as the field is applied and the system is tuned away from the CT. At the CT, we find a maximum coherence time of $1.05(3) \mu\text{s}$.

T_2 can be enhanced by employing the Carr-Purcell-

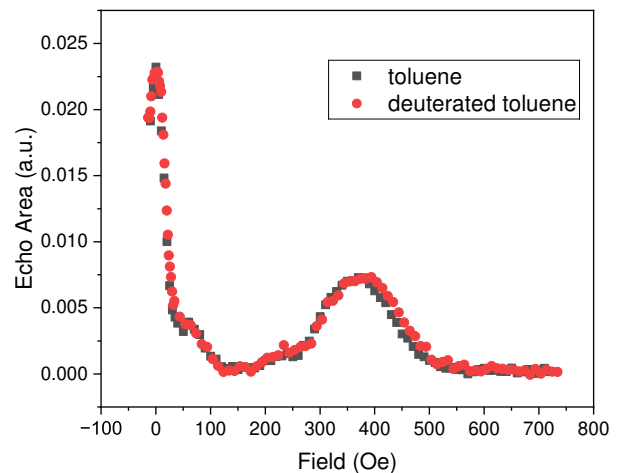


FIG. 3. Echo-detected field dependence. The spectra were obtained from liquid solution samples of 1% dilution of **2** in toluene (black) and deuterated toluene (red) at 1.8 K, and 3916 MHz and 3961 MHz, respectively. The peaks at zero field and at ~ 390 Oe are due to the CT and ESEEM, respectively. Both peaks are observed in spectra taken at various frequencies and are independent of the molecule's cation, the solvent used, or the cooling procedure. The delay time τ in the Hahn sequence used was 600 ns. The position and height of the ESEEM peak changes with the value of τ employed, as discussed in the main text.

Meiboom-Gill (CPMG) pulse sequence, whereby the spins are repeatedly refocused via repeated π pulses with uniform spacing 2τ , producing echoes at time τ after each π pulse. Each progressive echo area is smaller than the previous echo area; the exponential decay of the echoes during the CPMG sequence allows us to extract a value of T_2 . Fig. 4(b) shows an overlay of T_2 measured with a Hahn sequence (black) and a CPMG sequence (blue), with separate axis scales for each set of data. Both methods show a similar behavior in how the coherence time changes with field around the CT, but the CPMG method produces T_2 values that are approximately 2.8 times larger.

Fig. 5 shows T_2 as a function of the delay time τ obtained using the CPMG sequence. The effect of the CPMG sequence at the CT is shown in black. For small values of τ , we obtain a T_2 value of $2.62(7) \mu\text{s}$. We observe that T_2 drops somewhat for $\tau \gtrsim 1 \mu\text{s}$, which confirms that CPMG works by filtering low-frequency decoherence [53], and gives some insight on the noise spectra in our system: that a significant portion of the noise is below ~ 1 MHz.

We next turn to the behavior near the second peak in Fig. 3. Fig. 6(a) shows the echo area as a function of 2τ for fields in the vicinity of that peak obtained using a Hahn sequence. The echo signal oscillates with 2τ and the observed frequencies of oscillations matches well with the expected Larmor frequency of the proton at the corresponding field values, indicating the hyperfine origin of the oscillations. We collected oscillatory data at numer-

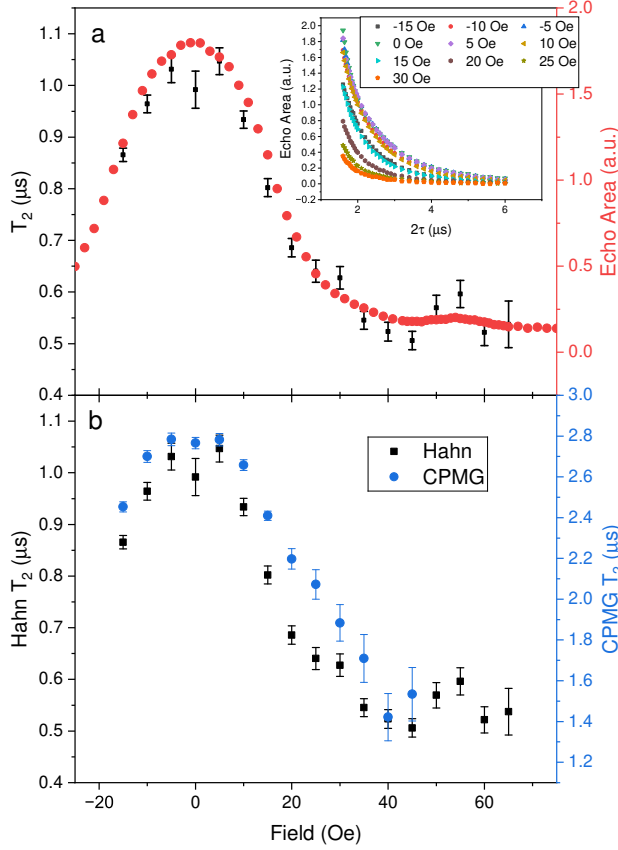


FIG. 4. T_2 values near the CT. a) EDfS data (red) and Hahn T_2 (black). The inset shows echo area as a function of 2τ for several values of magnetic field, as indicated. Fitting these curves to an exponential decay yields the T_2 values given in the main portion of the panel. The similarity in shape of the field dependence of the signal size and T_2 can be attributed to the reduction in T_2 as the field tunes the system away from the CT. The maximum value of T_2 is found to be $1.05(3)$ μs. b) T_2 measured with the CPMG pulse sequence (blue) overlaid with the values found using the Hahn sequence (black). The CPMG method yields values of $T_2 \sim 2.8$ times larger than those found using the Hahn sequence. The delay time τ used in the CPMG sequence was 800 ns. Data was taken with 5% dilution of **2** in toluene at 1.9 K and 4639 MHz.

ous field values and display the results in a contour map in Fig. 6(b), where echo amplitude, indicated by color, is plotted as a function of 2τ and field. The oscillations arise from hyperfine interactions manifesting as ESEEM [54]. The peak in echo signal occurs when $\omega_L \tau \approx 2\pi n$ and thus when $\tau \approx \frac{2\pi n}{\gamma_p B}$, using the Larmor frequency relation $\omega_L = \gamma_p B$, where γ_p is the nuclear gyromagnetic ratio of the proton. These ESEEM oscillations are the origin of the second peak in Fig. 3, which corresponds to the field for which $n = 1$. The curves in the contour map show the expected relation between 2τ and B_{peak} for several integer values of n , indicating good agreement with the positions of the echo amplitude maxima. We note that while we assume that ESEEM is due to interactions with

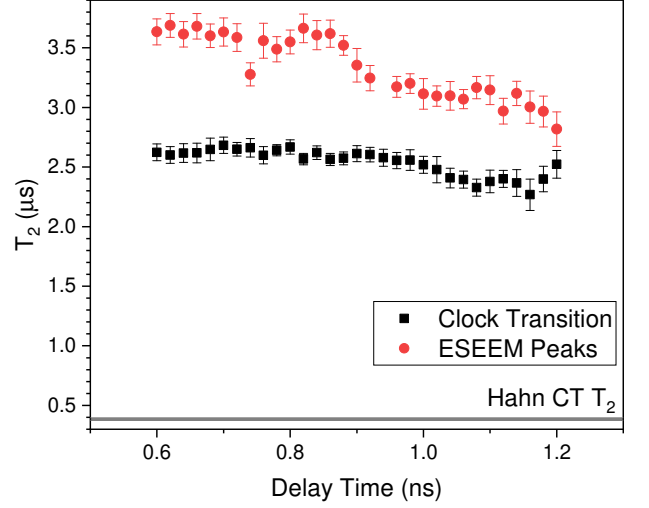


FIG. 5. τ dependence of T_2 when using the CPMG sequence. T_2 at CT (black points) is ~ 2.6 μs at small τ and falls off slightly for $\tau \gtrsim 1$ μs. The CPMG sequence was used to measure T_2 (red points) at the field for which τ suppressed the ESEEM oscillations – see Fig. 7. Measurements are from a 5% dilution sample of **2** in toluene at 5636 MHz and 1.8 K. The Hahn CT T_2 value indicated by a horizontal line near the bottom of the figure was measured along with the CPMG data.

protons, consistent with what others have seen in similar heterometallic rings [40], the molecule also contains fluorine, which has a gyromagnetic ratio $\sim 6\%$ smaller than that of the proton. With just a small number of ESEEM oscillations observable at low magnetic fields, we cannot rule out that fluorine plays a role in the observations.

Because of the oscillatory nature of the signal in Fig. 6, extracting a value of T_2 is difficult to do rigorously. In the Sec. IV A, we present the results of simulations that allow us to fit the data to extract T_2 . For now, we fit the envelope of the ESEEM to estimate T_2 at the ESEEM peaks as shown in Fig. 6(a). We find the “coherence time” around $1.13(5)$ μs, which indicates in this field range the coherence is comparable to that found at the CT. Furthermore, we can employ the CPMG technique to dynamically decouple the electronic and nuclear spin dynamics and demonstrably enhance T_2 [55]. Fig. 7(a) illustrates this technique at a single field of 295 Oe. The yellow curve shows the Hahn-echo-measured ESEEM oscillations as a function of 2τ . We measure CPMG with τ set to match the Larmor period – so that our π pulses are applied at the minima of the ESEEM oscillations in the Hahn data. The resulting echo amplitudes, represented by the black squares in the figure, show that with this choice of τ the oscillations are no longer observable and the signal decays approximately exponentially. One can immediately see that the system’s coherence has been extended through this technique since the echo amplitude obtained from CPMG is visible for a much longer time than when measured using the Hahn technique. A fit

yields a value of T_2 of $3.96(1) \mu\text{s}$ for this sample.

We repeat this procedure for several fields using a similar sample, with the value of τ equal to the corresponding Larmor period. The value of T_2 extracted from each experiment is plotted as a function of field in Fig. 7(b), showing an increase in T_2 from ~ 3.0 to $\sim 3.7 \mu\text{s}$ as field increases. The same data, plotted as a function of τ instead of field, is shown as red dots in Fig. 5. Notably, these values are all markedly larger than the values of T_2 obtained at the CT using the CPMG technique. Below we will present a similar conclusion from an analysis of our Hahn data.

Summarizing the main findings in this section, we have shown that coherence in our Cr_7Mn system can be significantly enhanced at a zero-field CT and by an ESEEM process. This is despite the broad inhomogeneity in the sample, since limited energy diffusion allows us to coherently manipulate a small sub-ensemble. Using a period-matched CPMG pulse sequence, we dynamically decouple the electronic spin from the protons contributing to ESEEM, suppressing the oscillations and resulting in an enhanced coherence time. The observed behavior of this system near the CT is independent of variation in sample cation. Moreover, the protons in the solvent and intermolecular distance do not have much effect on coherence or ESEEM behavior, suggesting that decoherence processes in this system are dominated by sources within the molecule.

IV. SIMULATIONS – INSIGHTS INTO DECOHERENCE FROM DATA

To gain a better understanding of our data and of the underlying sources of decoherence affecting the system, we performed simulations of the dynamics. The simulations, along with fitting to the data, allowed us to extract information about decoherence both near the CT and in the ESEEM regime. Because of the prominent ESEEM in our data, simulations include coupling of the electronic spin with nuclear spins. In this work, we treat ESEEM through two approaches: coherent coupling of the electronic spin to a (set of) neighboring nuclear spin(s), and treatment of the nuclear spins as an environmental source of magnetic noise. While the former is approach is conceptually more straightforward, the latter is more expansive, allowing for the inclusion of incoherent noise sources that lead to decoherence.

Standard treatments of ESEEM often involve a simple model of a $S = 1/2$ electronic spin coupled to an $I = 1/2$ nuclear spin. Such a model can be solved analytically [56]. Here, we consider an $S = 1$ system that has anisotropy and a CT. This complicates the coupling to nuclear spins and requires careful treatment.

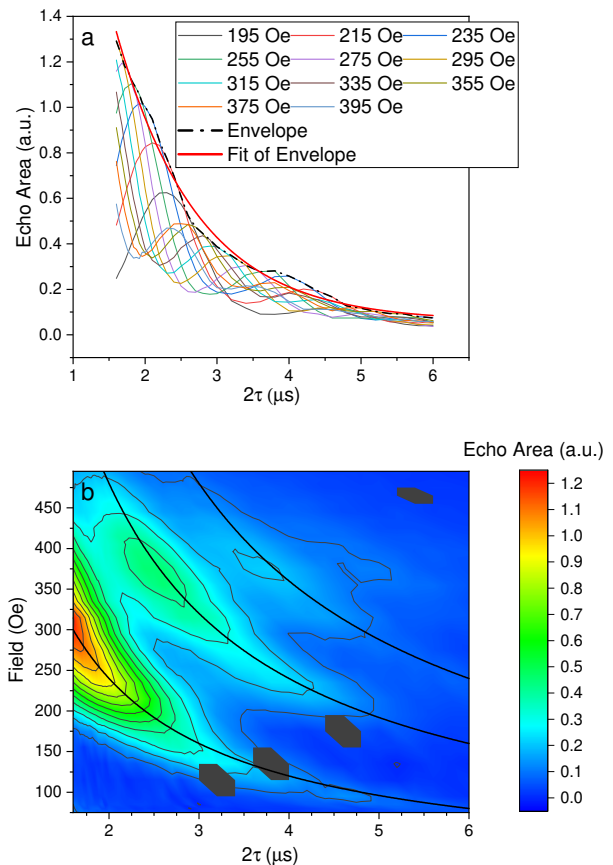


FIG. 6. ESEEM as a function of delay time and field. a) Echo area as a function of 2τ at several field values, as indicated. The observed oscillations have frequencies that agree with the proton Larmor frequencies at the corresponding fields. The envelope of modulated data suggests that T_2 in this range of field does not change significantly and is comparable to the value around the CT. b) Contour map of the echo area as a function of 2τ and field value. Echo area is indicated by color. The dark black lines mark the loci where $\gamma_p B \tau = 2\pi n$, the expected position of the echo amplitude maxima, showing good agreement with data collected. Grey hexagons indicate places where data is missing due to control issues with the experimental apparatus. Measurements were taken on a 5% dilution sample of **2** in toluene at 1.9 K and 4639 MHz.

A. ESEEM – a coherent approach

A first approach to quantitatively treating our ESEEM results employs the following Hamiltonian

$$\mathcal{H} = -DS_z^2 + E(S_x^2 - S_y^2) + g_s \mu_B \mathbf{B} \cdot \mathbf{S} - g_p \mu_p \mathbf{B} \cdot \mathbf{I} + A_{zz} S_z I_z + A_{zx} S_z I_x + A_{zy} S_z I_y, \quad (2)$$

which in addition to Eq. 1 contains secular (A_{zz}) and pseudo-secular (A_{zx} , A_{zy}) hyperfine terms, as well as a nuclear Zeeman term. In calculating the dynamics of this model, we take into account the various forms of inhomogeneity of the system.

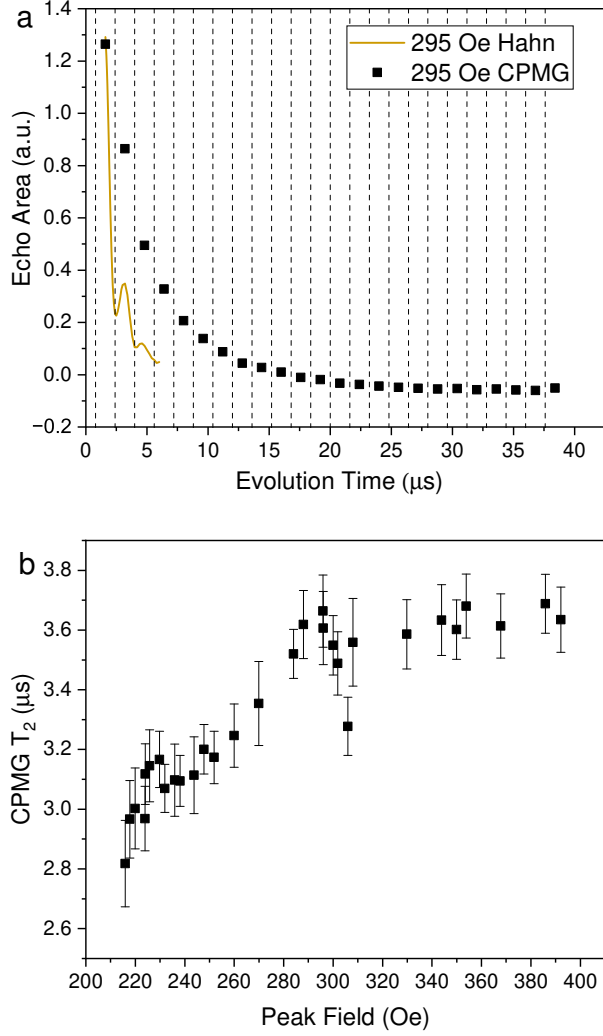


FIG. 7. CPMG demodulation of ESEEM. a) Illustration of the decoupling technique at 295 Oe. The yellow curve shows the Hahn-echo-measured ESEEM oscillations as a function of τ . In our CPMG technique τ was set to match the Larmor period so that our π pulses are applied at the minima of the ESEEM oscillations in the Hahn data. The black points are the echo data obtained from this CPMG sequence; CPMG signal decays slower than that from the Hahn sequence. The dashed vertical lines indicate the times of the π pulses used in the CPMG sequence. The sample used for these measurements was a 5% dilution of **2** in toluene at 1.9 K and 4639 MHz. b) T_2 measured with the corresponding CPMG sequence at different field values with the technique illustrated in a). These measurements were carried out on a similar sample but at 1.8 K and 5636 MHz.

As illustrated in Fig. 1, there is substantial inhomogeneity in the transverse anisotropy E of the spins. In addition, the use of solution samples in this study introduces orientational disorder to the system. Both the ESR transition frequency and transition matrix element depend on the molecule's orientation relative to the field. Thus, each sample contains a wide range of transition

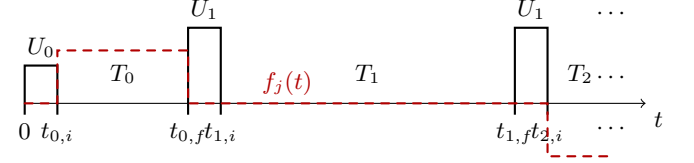


FIG. 8. Schematic of CPMG- N pulse sequence. The notation used in simulation is illustrated and an example of $f_j(t)$ (see Sec. IV B) is shown. Note that since we treat pulses as infinitesimal, no noise-induced phase is accumulated during a pulse, hence $f_j(t) = 0$ for all pulses.

frequencies – wider than the bandwidth of the resonator. This orientational disorder creates a complicated relationship between signal and molecular parameters that ultimately requires numerical modeling.

Despite the variety of orientations, the expected ESR signal in parallel mode is always along the direction of DC field. The direction of the field in the molecule's frame is along the direction \hat{n} and we are interested in the component of spin along this direction, $S_n \equiv \mathbf{S} \cdot \hat{n}$.

For any given spin in our ensemble, we calculate the dynamics of the quantum mechanical expectation value $\langle \hat{S}_n \rangle = \text{tr}(\rho \hat{S}_n)$. However, we also need to account for the various forms of inhomogeneity in the spin ensemble. We define the ensemble average \overline{X} as the average of X over the inhomogeneities in the sample, e.g. random orientation of molecules as well as inhomogeneity in E . The ensemble average of $\langle S_n \rangle$ is thus

$$\begin{aligned} \overline{\langle S_n \rangle} &= \frac{1}{4\pi} \int d\Omega \int dE \lambda(E) L(\epsilon) \langle S_n \rangle \\ &= \frac{1}{4\pi} \int d\Omega \int d\epsilon \left| \frac{\partial \epsilon}{\partial E} \right|^{-1} \lambda(E) L(\epsilon) \langle S_n \rangle, \end{aligned} \quad (3)$$

where $L(\epsilon) = \left\{ [2(\epsilon - \epsilon_0)/\Gamma]^2 + 1 \right\}^{-1}$ is the lineshape function for the experimental resonator with ϵ , ϵ_0 and Γ being the spin transition frequency, the resonator frequency and resonator linewidth, respectively. $\lambda(E)$ is the distribution of the transverse anisotropy parameter E , which we take to be sufficiently broad to be treated as a constant. The bounds of integration for ϵ are such that the entirety of the LGR's resonance is included, since only near-resonance signal is detected in the experiment. Finally, an integral over the solid angle $d\Omega$ considers all possible orientations of the molecule in the solution.

The dynamics of this model are implemented by assuming the system is initially in a pseudo-pure ground state, calculating the density matrix evolution $\rho(t) = U_t \rho(0) U_t^\dagger$ in the rotating frame of the radiation field, and then calculating $\langle S_n \rangle$. In the case of the CPMG sequence with N π pulses (i.e., CPMG- N), the time evolution operator, $U_t = (U_\tau U_1 U_\tau)^N U_0$, includes evolution due to the radiation pulses (U_0 and U_1 – see Fig. 8) as well as free evolution between pulses (U_τ). The value of $\langle S_n \rangle$ is then averaged over the distribution in E and in

orientations (Eq. 3) to produce a dependence of echo size on experimental variables like field and time. We add *ad hoc* pure dephasing by multiplying the calculated time dependence with an exponential decay e^{-t/T_2} with T_2 a free parameter that depends on field. Other parameters in our fitting are hyperfine coupling constants A_{zz} and $A_{z\perp} \equiv A_{zx}$ (setting $A_{zy} = 0$, without loss of generality, due to symmetry), as well as an overall scaling factor.

This model works reasonably well in replicating our experimental data at fields near the CT and in the range 195–395 Oe. Figure 9(a) shows a comparison of the experimental and simulated dependence for several fields near the CT. Unsurprisingly, in this regime no oscillations are observed since the Larmor frequency is very low. For fields in the range 195–395 Oe, a 3D contour map of the simulation with the best-fit parameters is shown in Fig. 9(b) and compares favorably with the data (Fig. 6) within the region of fields shown.

Figure 9(c) shows the T_2 values determined from fitting at fields near the CT and at higher fields, excluding a range of fields where the fitting fails to match the data, discussed in more details below. There are clearly two peaks in T_2 : around the CT and in the vicinity of 300–400 Oe. Interestingly, we observe that the value of T_2 is somewhat larger at this second peak than at the CT (the smaller echo area is due to smaller matrix elements, i.e. the undecohered signal is smaller). This is consistent with our finding that T_2 measured through CPMG is larger when measured in the ESEEM regime than at the CT (Fig. 5), but here we see this enhancement even without the dynamical decoupling provided by the CPMG sequence. This points to a difference in decoherence mechanisms at play in the two regimes: at zero field, the spin is immune to field fluctuations to first order and decoherence is driven by second-order fluctuations or fluctuations of a non-magnetic origin. At zero field, the nuclear spins have no Larmor precession and thus have incoherent dynamics. On the other hand, in the ~ 300 –400 Oe range, the nuclear spins have coherent Larmor precession, resulting in the observed ESEEM. This coherent precession may make the overall system dynamics more reversible, extending T_2 in this field range.

Despite the success of this model near the CT and at higher fields, it fails to reproduce the observed behavior in the intermediate field range of ~ 50 –200 Oe – see [49]. The signal size in this range of fields is approximately an order of magnitude smaller than in the higher-field range, something that we cannot adequately reproduce with the model presented above.

In our fitting, we treated T_2 as a fitting parameter. However, T_2 is not a fundamental parameter, but a reflection of an underlying decoherence process. Such processes cannot generally be encapsulated by a single parameter. Thus, we turn to a more general approach to characterize how the environment gives rise to decoherence. In this approach, we characterize the environment as the source of a field-dependent noise spectrum seen by the electronic spin.

To gain insight into this environmental noise and how it affects the dynamics of the electronic spin, we took detailed CPMG data with many values of τ , a selection of which are shown in Fig. 10. (Additional data at other fields are provided in [49].) Some recent studies have used such an approach with large numbers of π pulses to extract information about the noise spectrum of the environment [57–61]. However, for the range of τ values accessible in our experiments, echoes from after more than three π pulses often had a poor signal-to-noise ratio, preventing us from implementing this approach directly. Instead, we used a physically motivated environmental noise model to simultaneously fit our CPMG-1 through CPMG-3 data, glean information about noise sources that underlie the observed behavior and decoherence.

B. General approach to modeling decoherence

We develop a phenomenological model of the noise as a function of field that includes a nuclear-spin bath, as well as noise in the molecule’s transverse anisotropy. Using this model, we are able to extract information about the noise spectrum seen by the electronic spin that contributes to its decoherence.

The complications arising from the system’s inhomogeneities still require averaging using Eq. 3. However, here we need an additional average to deal with the noise: $E[\dots]$ denotes the average of the decohering effects of noise. Including this average into our calculations changes our expected signal from $\langle S_n \rangle$ to $E[\langle S_n \rangle]$.

To find $E[\langle S_n \rangle]$, the decohered (noise ensemble averaged) expectation value of our signal along the DC field direction for a given value of E and given orientation \hat{n} , we implement the following process. We treat our $S = 1$ system as an effective two-level system, where the two lowest energy eigenstates, $|\psi_0\rangle$ and $|\psi_1\rangle$, are the pair involved in the CT at zero field and are resonant with the applied radiation. (At zero field, $|\psi_0\rangle = |-\rangle$ and $|\psi_1\rangle = |+\rangle$.) We work in a rotating frame and employ the rotating-wave approximation so that the only time dependence in the Hamiltonian is produced by the noise during periods of free evolution. The dynamics of this system are described by the time-evolution operator: $\rho(t) = U(\delta\epsilon, t) \rho(0) U^\dagger(\delta\epsilon, t)$, where $\delta\epsilon(t) = \epsilon - E[\epsilon]$ is the noise in transition energy ϵ . We are interested in calculating $\langle S_n \rangle = \text{tr}(\rho(t) S_n)$ after time evolution. Any state in the two-level eigenbasis can be represented as $\Psi = \alpha |\psi_0\rangle + \beta |\psi_1\rangle$. It is then straightforward to show that $\langle S_n \rangle = 2 \Re(\alpha \beta^* \langle \psi_1 | S_n | \psi_0 \rangle)$.

We wish to find the time evolution of the system after any number $N + 1$ of radiation pulses (e.g. CPMG- N sequence). Following the same procedure discussed in coherence Sec. IV A, the evolution is broken up into that produced by pulses and free evolution during interpulse time intervals, which we denote $T_m \equiv (t_{m,i}, t_{m,f})$, $m = 0, 1, \dots$, as illustrated in Fig. 8. We treat the pulses as infinitesimally short, but not as perfect π or $\pi/2$ pulses

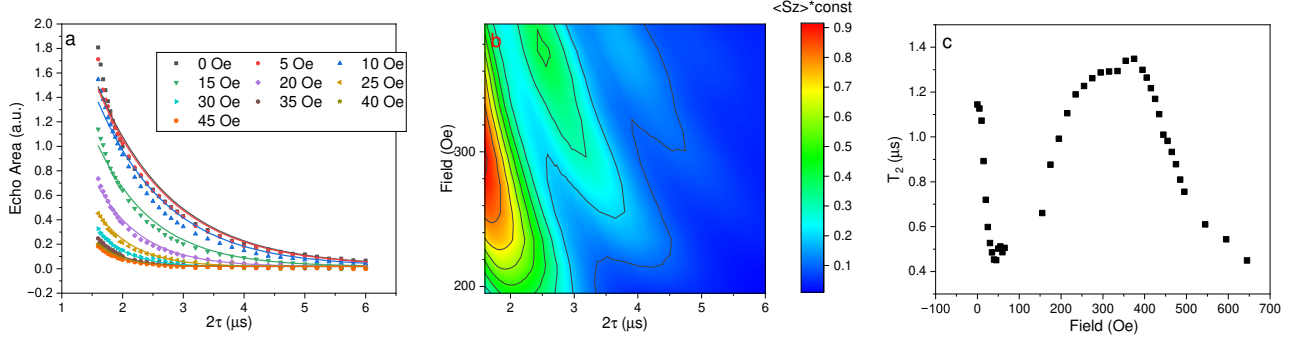


FIG. 9. Fitting results in the fields around CT and 195 – 395 Oe. In the simulation, we used infinitesimal pulses and free evolution with pure dephasing. The hyperfine parameters found with this fitting is $A_{zz} = 5.72$ MHz, $A_{z\perp} = 0.515$ MHz. a) Fitting (solid lines) of data (points) at fields near the CT. T_2 for each field value is treated as a free fitting parameter. b) Contour map of the simulated signal as a function of 2τ and field in range 195 – 395 Oe. c) T_2 values extracted from fitting of data as a function of field.

due to the inhomogeneity in E and molecule orientation – different spins in the ensemble will undergo different rotations. The inclusion of noise during inter-pulse intervals introduces additional complexity for a non-ideal sequence. In particular, the accumulated phase due to noise is mixed in a nontrivial manner. For a given value of E , spin orientation, and noise history $\delta\epsilon(t)$, the dynamics of $\langle S_n \rangle$ reduces to

$$\langle S_n \rangle = \sum_j A_j \cos \phi_j, \quad (4)$$

where A_j are constants that depend only on the pulses and ϕ_j is the accumulated noise-induced phase. $\phi_j = \sum_m a_{m,j} \int_{T_m} dt \delta\epsilon = \int_T dt \delta\epsilon f_j(t)$, defining $f_j(t) = \sum_m a_{m,j} \Theta(t - t_{m,i}) \Theta(t_{m,f} - t)$, where $\Theta(t)$ is the Heaviside step function, and $a_{m,j}$ is the weight of the phase accumulation for during the free-evolution time interval T_m . Fig. 8 shows an example of $f_j(t)$ in which $\{a_m\}_j = \{1, 0, -1, \dots\}$. With $N + 1$ pulses, $m = 0, 1 \dots N$ for $N + 1$ intervals. Each $a_{m,j}$ can be 0 or ± 1 for $m < N$. With these three possible values as well as the fact that $a_{N,j} = -1$ always (the accumulated phase in the last free evolution interval does not get mixed, as shown in example below), Eq. 4 has at most 3^N unique terms.

As an example of the above procedure, we consider the two-pulse “Hahn” sequence, where the two periods of free evolution both have duration τ . The evolution of the system initially in the ground state is described by the

following.

$$\begin{aligned} \begin{pmatrix} 0 \\ 1 \end{pmatrix} &\xrightarrow{U_0} \begin{pmatrix} U_0^{00} & U_0^{01} \\ U_0^{10} & U_0^{11} \end{pmatrix} \cdot \begin{pmatrix} 0 \\ 1 \end{pmatrix} = \begin{pmatrix} U_0^{01} \\ U_0^{11} \end{pmatrix} \\ &\xrightarrow{U_\tau} \begin{pmatrix} U_0^{01} \\ U_0^{11} e^{i \int dt_0 \epsilon} \end{pmatrix} \\ &\xrightarrow{U_1} \begin{pmatrix} U_1^{00} U_0^{01} + U_1^{01} U_0^{11} e^{i \int dt_0 \epsilon} \\ U_1^{10} U_0^{01} + U_1^{11} U_0^{11} e^{i \int dt_0 \epsilon} \end{pmatrix} \\ &\xrightarrow{U_\tau} \begin{pmatrix} U_1^{00} U_0^{01} + U_1^{01} U_0^{11} e^{i \int dt_0 \epsilon} \\ U_1^{10} U_0^{01} e^{i \int dt_1 \epsilon} + U_1^{11} U_0^{11} e^{i(\int dt_0 + \int dt_1) \epsilon} \end{pmatrix} \\ &\equiv \begin{pmatrix} \alpha \\ \beta \end{pmatrix} \end{aligned} \quad (5)$$

For this case, we see $\alpha\beta^*$ (used to calculate $\langle S_n \rangle$) can be reduced to a sum of three terms (three values of j), corresponding to the three possible combinations of $\{a_0, a_1\}_j$, i.e. $\{-1, -1\}$, $\{1, -1\}$, and $\{0, -1\}$. After absorbing the phase due to $E[\epsilon]$ into the A_j ’s, we have three unique noise-induced phases ϕ_j : $-\int dt_0 \delta\epsilon - \int dt_1 \delta\epsilon$, $\int dt_0 \delta\epsilon - \int dt_1 \delta\epsilon$, and $-\int dt_1 \delta\epsilon$. As more pulses are added, e.g. for a CPMG- N sequence, each will increase the number of terms in Eq. 4.

Once $\langle S_n \rangle$ is determined (Eq. 4), one can then calculate $E[\langle S_n \rangle]$, assuming the noise has a Gaussian distribution with no temporal correlation, by using the well-known relation $E[\cos \phi] = \exp(-\frac{1}{2} E[\phi^2])$, yielding

$$E[\langle S_n \rangle] = \sum_j A_j e^{-\chi_j}, \quad (6)$$

where

$$\begin{aligned} \chi_j &= \frac{1}{2} E[\phi_j^2] = \frac{1}{2} \iint_T dt dt' E[\delta\epsilon(t) \delta\epsilon(t')] f_j(t) f_j(t') \\ &= \int_0^\infty \frac{d\omega}{2\pi} S_\epsilon(\omega) \left| \int_T dt e^{i\omega t} f_j(t) \right|^2. \end{aligned} \quad (7)$$

Here $S_\epsilon(\omega) \equiv \int dt e^{i\omega t} E[\delta\epsilon(0)\delta\epsilon(t)]$ is the spectral density of the noise $\delta\epsilon$. We define

$$\mathcal{F}_j = \omega^2 \left| \int_T dt e^{i\omega t} f_j(t) \right|^2, \quad (8)$$

which is commonly known as a filter function and is dependent on the particular pulse sequence described by f_j . CPMG (as well as other multi-pulse sequences) has a well-known filter function that can be used to analyze the dynamics of the experimental echoes to recover the underlying noise spectrum [53, 60, 62, 63].

C. Noise Sources – Fitting the data

We consider that the electronic spin sees two sources of noise: one due to a nuclear spin bath and the other due to fluctuations in the anisotropy parameter E , which determines the CT frequency at zero field. Most treatments of decoherence in MNMs focus on the effects of the spin bath [58, 63–70]. However, at the CT, decoherence from the spin bath is minimized, allowing other, non-magnetic sources of noise to dominate the decoherence. We thus consider a form of noise that would remain if all magnetic fluctuations were absent: fluctuations in E , which could arise from dynamical conformational changes in the molecule. Given the large inhomogeneity in E in this system, fluctuations in the parameter are unsurprising. We assume these fluctuations in E to have a $1/f$ spectrum. It is important to note that noise in E cannot be filtered by the CT and so will always give rise to decoherence. Importantly, we find that omitting the fluctuations in E from our model results in a substantially worse fit to our zero-field data (see [49]).

Spin bath noise is modeled as arising from a collection of nuclear spins (protons with $I = \frac{1}{2}$), which we treat as isotropically distributed for simplicity. Each nuclear spin is taken to have a random orientation and to be uncorrelated with all other spins in the bath. It produces a dipole magnetic field at the location of the electronic spin that depends on its location in space. The total dipolar fluctuating field from the entire bath of nuclear spins at the electronic spin is dubbed \mathbf{B}_I . We treat \mathbf{B}_I as a classical field. Thus, the spin Hamiltonian becomes

$$\mathcal{H} = -DS_z^2 + E(S_x^2 - S_y^2) + g_s\mu_B(\mathbf{B}_{\text{ext}} + \mathbf{B}_I) \cdot \mathbf{S}. \quad (9)$$

The spectrum of the fluctuations in \mathbf{B}_I is determined from the following simple model. Each nuclear spin has a random initial state and precesses at its nuclear Larmor frequency ω_L around the total instantaneous field \mathbf{B}_{ext} . We assume white-noise fluctuations in ω_L (reflecting interactions between bath spins). This, in turn, produces fluctuations in \mathbf{B}_I , with a Lorentzian spectrum with a central frequency $\omega_{L,0}$, corresponding to the mean value of field B_{ext} . Near the CT, ϵ has a non-linear dependence on field. Expanding this dependence in a Taylor series and keeping terms up to order \mathbf{B}_I^2 results in a noise spectrum in ϵ with peaks at $\omega_{L,0}$ and $2\omega_{L,0}$.

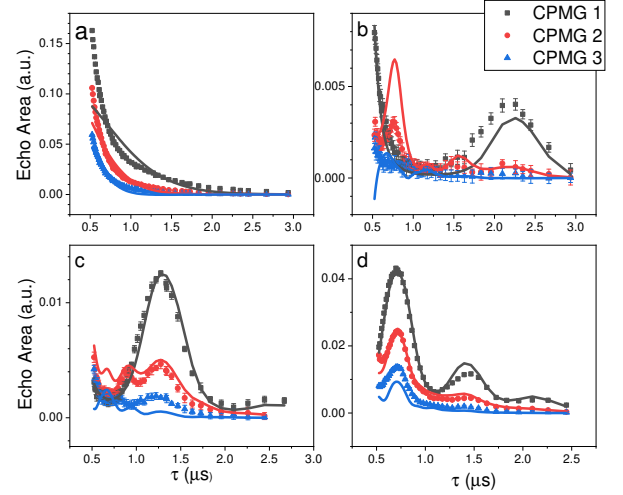


FIG. 10. CPMG data (points) and fits (solid lines) at fields of (a) 0, (b) 100, (c) 175, and (d) 325 Oe. The sample is a 10% toluene solution of **2** at 1.8 K and 4730 MHz.

Solving for the state energies from Eq. (9), we can infer how the temporal autocorrelation function of energy ϵ relates to correlation functions of E , as well as those for components of vector \mathbf{B}_I , and tensor $\mathbf{B}_I \otimes \mathbf{B}_I$. After averaging over the angular distribution of the spin bath and the random orientation of the nuclear spins, we obtain three “conversion coefficients” C_i , which are derived from the model before fitting, for any given specific anisotropy E and \mathbf{B}_{ext} (see [49] for details). Combining these noise sources, one obtains a total noise spectral density of

$$S_\epsilon(\omega) = C_1 S_{B_I} + C_2 S_{\mathbf{B}_I \otimes \mathbf{B}_I} + C_3 S_E, \quad (10)$$

where

$$S_{B_I}(\omega) = \alpha \int dt e^{i\omega t} \cos(\omega_{L,0}t) e^{-\frac{1}{2}\sigma t}, \quad (11)$$

$$S_{\mathbf{B}_I \otimes \mathbf{B}_I}(\omega) = \beta \int dt e^{i\omega t} \cos(2\omega_{L,0}t) e^{-2\sigma t}, \quad (12)$$

$$S_E = \gamma \cdot \frac{1}{\omega} \quad (13)$$

where α , β , γ and σ are parameters to be fit. α and β contain information about the radial distribution of the spin bath, γ represents the noise amplitude of fluctuations in E , and σ represents the magnitude of the fluctuations in ω_L . The fitting parameters α and σ are taken to depend on the magnitude of \mathbf{B}_{ext} while γ , β and a scaling factor are treated as being independent of field.

Figure 10 shows results of simultaneously fitting data from CPMG-1, CPMG-2 and CPMG-3, using all fields characterized in a single sample. For clarity, the figure shows results for fields of 0, 100, 175 and 325 Oe, as indicated. (Results of fitting at other fields are shown in [49].) There is good quantitative agreement at the two higher fields. The basic oscillatory structure is well reproduced at 100 Oe for both CPMG-1 and CPMG-2 even

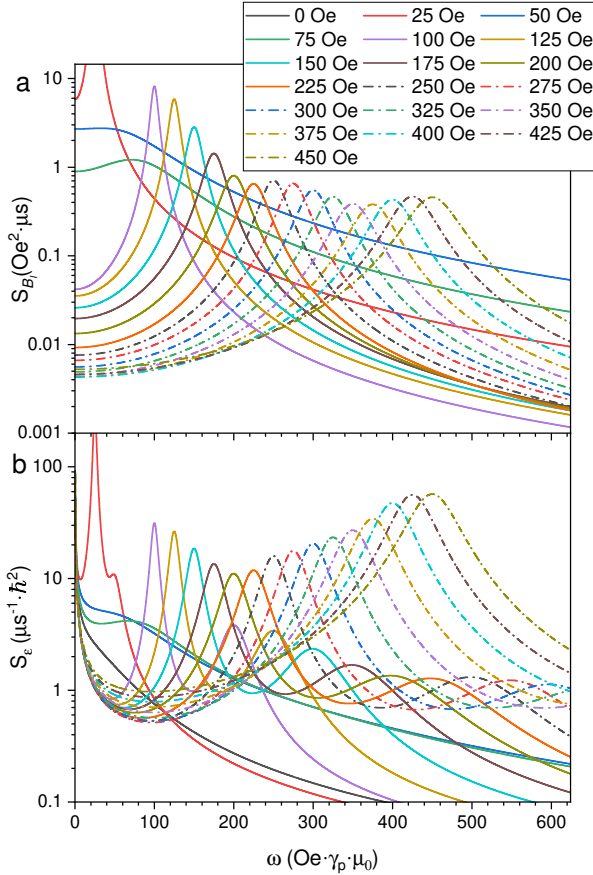


FIG. 11. Noise spectra at different fields. a) $S_{B_I}(\omega)$ shows a single peak at the Larmor frequency. Note that no noise spectrum is shown for $B = 0$ since it is effectively filtered out by the CT and therefore cannot be inferred from the experimental data. b) $S_{\epsilon}(\omega)$ determined from Eq. 10, calculated using the specific orientation that gives the largest contribution to the echo signal.

though the fit does not reproduce the data quantitatively. At certain fields, the simulations produce an additional peak (e.g. $\tau \sim 0.7 \mu s$ in Fig. 10c) for CPMG-2 not seen in the data.

We note that at zero field, the noise is dominated by fluctuations in the anisotropy E since the CT effectively filters out field fluctuations. It may be surprising that the zero-field data is not reproduced well by the simulations since that behavior appears to be close to exponential. Indeed, one can fit, say, CPMG-1 alone and get a good fit, but the noise spectrum extracted will not reproduce the CPMG-2 or CPMG-3 behavior satisfactorily. This suggests that our model of treating the E fluctuation spectrum as having a $1/f$ character does not fully capture the physics. We attempted other realistic models, such as a $1/f^2$ spectrum or adding white noise to the $1/f$ spectrum, without appreciable improvement.

Our fitting yields several parameters: one value of α and one value of σ for each value of B_{ext} , and a single value for each of β , γ , and a scaling factor. From these

parameters, we can calculate the components of the noise spectrum at each field (Eq. 10). Fig. 11a shows the magnetic field component of the noise spectrum, S_{B_I} , for several values of B , as indicated. Notably, the amplitude of the Larmor peak (at $\omega_{L,0}$) is roughly constant for all fields above ~ 200 Oe.

Figure 11(b) shows the full noise spectrum S_{ϵ} , containing all three components in Eq. 10. Since the conversion coefficients C_1 and C_2 depend on the orientation of the molecule with respect to the field direction, Fig. 11(b) shows the spectrum that corresponds to the molecule orientation that yields the largest contribution to the echo signal for a given field. Other orientations yield similarly shaped spectra, but with different amplitudes for the Larmor and $1/f$ components. In the noise spectra shown, most fields show a prominent peak at $\omega_{L,0}$ (due to S_{B_I}), and a significantly smaller peak at $2\omega_{L,0}$ (due to $S_{B_I \otimes B_I}$), as well as the $1/f$ behavior at the lowest frequencies. In contrast to Fig. 11(a), in S_{ϵ} we see that the overall area of the Larmor peak tends to steadily decrease with decreasing field (although for fields in the 100 – 200 Oe range the width of this peak is substantially narrowed). This reflects the influence of the CT, where magnetic field noise is more effectively filtered out as the field approaches zero. The spectra at fields < 100 Oe seem to vary widely with field, with σ being anomalously large for 50 and 75 Oe. Unsurprisingly, it is in this same field range where the fits have only modest agreement with the data and so the inferred noise spectra may not fully represent the physics at those fields. Attempts to constrain σ to values similar to those found at larger fields yielded substantially worse agreement with the data.

The observed behavior of our data as a function of field and delay time τ can be understood in terms of the filtering of the noise spectrum by our pulse sequence. Each pulse sequence has an associated filter function, \mathcal{F} , cf. Eq. 8. For an ideal, two-pulse Hahn sequence (i.e. CPMG-1), the filter function is given by $\mathcal{F} = 16 \sin^4 \frac{\omega \tau}{2}$. In Fig. 12, we overlay the noise spectrum S_{ϵ} at 300 Oe with the filter function \mathcal{F} for various values of τ used in our experiments. The filter function has a “notch” when $\omega = 2\pi/\tau$; noise at this frequency is filtered out very effectively. When the notch overlaps with the Larmor peak in S_{ϵ} , the decoherence produced by that peak in the spectrum is significantly reduced, resulting in a large echo signal, as shown in the lower panel of the figure. As τ is varied, the effectiveness of this filtering is modulated, resulting in the oscillatory behavior characteristic of ESEEM. Note that this behavior does not rely on any intrinsic coherent coupling between the electronic spin and nuclear spins, but arises from simply treating the nuclear spins as the source of incoherent field-noise fluctuations peaked at the nuclear Larmor precession frequency.

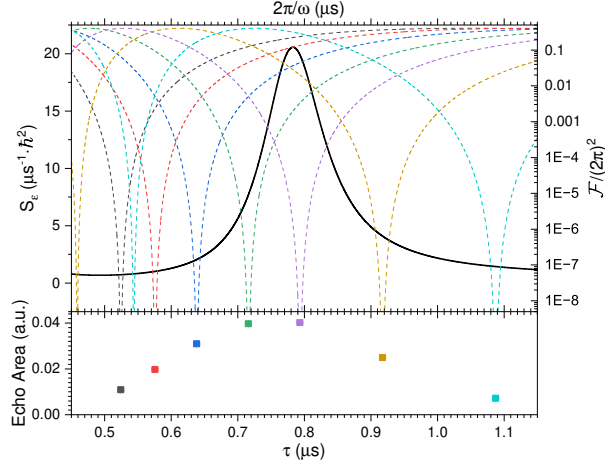


FIG. 12. Illustration of ESEEM oscillations produced through filtering of noise. The black curve in the top panel is the noise spectrum at 300 Oe as a function of $2\pi/\omega$. The dashed lines indicate the Hahn (i.e. CPMG-1) filter function \mathcal{F} for different values of delay τ ; dips occur when $\omega = 2n\pi/\tau$. Values of τ chosen for the filter functions correspond to ones used in the experiment. When the dip of a filter function overlaps substantially with the peak in the noise spectrum, the noise is effectively filtered out. The lower panel shows measured echo area as a function of τ at 300 Oe. When there is substantial noise filtering by the filter function, a significantly larger echo signal is observed.

V. DISCUSSION

There are a few notable conclusions we can attain from our results. One is that decoherence near the CT is primarily caused by noise sources arising within the molecule itself. This conclusion is supported by two findings: 1) We see very little change in behavior when we dilute the molecules in toluene solvent. Solutions ranging from 0.1% to 10% have been studied without appreciable change in the echo’s observed dependency on field or in the T_2 values extracted. This implies that intermolecular interactions are not a significant form of decoherence. 2) Changing the solvent from regular toluene to deuterated toluene does not have any noticeable effect on our observations (see Fig. 3 and [49]). This suggests that the protons in the spin bath are within the molecule itself and not arising from the solvent matrix. This is consonant with previous work [34] on Cr_7Ni , which is a related ring but lacks a CT, that showed deuteration of solvent only had a substantial effect on coherence after the ligands had also been deuterated. The only form of long-range noise then that may give rise to decoherence would be spin-vibrational coupling, which is largely independent of dilution or of solvent deuteration.

Our noise spectrum model has two distinct components: spin bath fluctuations and anisotropy fluctuations. While the former may dominate for most spin qubits, the latter should be considered in systems that have CTs,

where the magnetic fluctuations can be effectively filtered. Indeed, fluctuations in the CT frequency itself may be the limiting source of decoherence for some CTs where the effects of the spin bath are minimized. In our model, the zero-field CT frequency is determined entirely by E . In other MNMs, the CT frequency is determined by other Hamiltonian parameters, such as elements of the hyperfine tensor, and the fluctuations in such parameters can lead to decoherence. Such non-magnetic fluctuations are likely vibrationally mediated and thus may be mitigated through chemical engineering to alter the vibrational properties of the molecules, working at lower temperature to freeze out vibrational modes, or exploiting symmetries that suppress spin-phonon coupling of certain modes.

In addition, our extracted noise spectra (Fig. 11) have strong dependence on field. While a zero-field CT is most effective in filtering field fluctuations when the external field is zero, that is also the condition for when the Larmor peak has moved to zero frequency. As we have shown, away from zero field, use of a period-matched CPMG sequence can effectively filter out the decohering effects of noise at the Larmor frequency. Such an approach cannot be employed at zero field where the nuclear spin dynamics are incoherent. Thus, the CT is the primary tool available for filtering both the noise from the spin bath and that of other magnetic degrees of freedom. If the noise from the nuclear spin bath could be substantially reduced by using, e.g., ligands with primarily $I = 0$ isotopes, decoherence from Larmor precession would be mitigated. The CT could then potentially be more effective at filtering out the remaining magnetic field noise.

The model we have developed of environmental noise, despite containing several heuristic and simplifying assumptions, demonstrates a remarkable ability to reproduce the key behaviors of the system. This suggests that the model captures the core mechanisms driving the system’s behavior. Since it is not very sensitive to specific microscopic configurations, the model has the potential to be applied to a broader family of systems (e.g., Cr_7Ni and other MNMs). It may serve as a flexible and extensible framework for understanding a wider range of related phenomena.

The simplifying assumptions used in our model may account for discrepancies between the model and the actual behavior of the system: First, we assume an isotropic distribution of nuclear spins whereas the ring-like shape of the molecule suggests that the proton spins have an anisotropic distribution. Second, the Larmor precession frequency of the nuclear spins is taken to have some noise, modeled through the parameter σ , but the precession is taken to occur only around the applied field direction. At low applied fields, this assumption may not be well justified and the precession axis direction may itself be subject to noise. Next, our model is effectively one of “pure dephasing,” in which the noise only changes the relative phase in our two-state system, but we do not consider noise-induced transitions between energy eigen-

states. Portions of our noise model, such as the $1/f$ character for S_E , have an *ad hoc* character. Finally, we treat our noise as uncorrelated. A more realistic, many-body approach to treating the environment, particularly that of the spin bath, would be to include correlations between nuclear spins, using, e.g., a cluster-correlation expansion approach [32, 66, 69, 71, 72]. Such an approach may provide an understanding of the environmental noise that is better grounded in the microscopic structure of the molecule.

We note that T_2 is found to be larger in the ESEEM regime than at the CT peak, when measured using both the Hahn (Fig. 9) and CPMG (Fig. 5) sequences. This perhaps surprising finding may be related to the nature of the nuclear spin dynamics: In the ESEEM regime, the nuclear spins have precession frequencies on the order of MHz. The contribution from this high-frequency field may be to add a modulation to the low-frequency noise, upconverting it to higher frequency, where it can be effectively filtered out by the pulse sequence. Modulation-induced upconversion of noise has been used as a technique to enhance coherence [70]. We suggest that something similar may be occurring in our system, albeit without an external modulation, but instead with the nuclear spin precession acting as a natural form of modulation. Thus, the enhancement of T_2 in the ESEEM regime may point to a built-in form of dynamical decoupling in the Cr_7Mn molecular nanomagnet.

Recent experimental studies have looked at CTs with frequencies well above X band [25, 73]. Such high-frequency CTs have the potential for longer coherence times since the curvature of the frequency's dependence on field gets smaller with higher frequency. The lower frequency of the Cr_7Mn CT, in contrast, has some experimental and practical advantages. Experimentally, these frequencies are readily synthesized, allowing precise control of pulse sequences, including the phase needed for CPMG and other sequences. Practically, the CT studied here is similar in frequency to what is used in many superconducting qubits. In tandem, superconducting qubits' performance is degraded by large applied magnetic field. Thus, the frequency range and low fields of MNM-based CTs may allow them to serve as elements in a hybrid quantum architecture [74–77], perhaps as part of a quantum memory, in which they are integrated with superconducting qubits. Thus, spin CTs with frequencies in the range of a few GHz are well suited for interfacing with superconducting qubits. MNMs like Cr_7Mn with low-frequency CTs are therefore attractive, potentially practical spin qubits.

VI. CONCLUSION

Our experiments reveal T_2 values in the few μs range, when enhanced by CT or in a portion of the ESEEM

oscillation field range. Dynamical decoupling with the CPMG pulse sequence leads to enhanced coherence in both regimes. Studying molecular-spin qubits in the vicinity of CTs demonstrate the enhancement of coherence in these systems and provide a window into the underlying microscopic origins of decoherence. In this study, through a combination of experimental data and theoretical modeling, we have found that decoherence in the Cr_7Mn molecular magnet is produced by nuclear-spin fluctuations, which can be substantially filtered by a CT, and fluctuations in the molecule's anisotropy, which cannot. In systems with CTs, the fluctuations in the CT transition frequency, whether arising from fluctuations in anisotropy or from other Hamiltonian parameters, may present a limit on the ultimate efficacy of CTs in enhancing coherence.

One of the major advantages of MNMs is the ability to chemically engineer their properties. Our findings about the decoherence sources in Cr_7Mn suggest ways to enhance coherence in this molecule and related MNMs. Thus, we conclude that minimizing hyperfine fields from the nuclear spin bath – even with the filtering offered by a CT – is important to reduce their decohering effects. In addition, stiffening the molecular structure or making other structural changes could reduce fluctuations in the CT frequency. Such design considerations should inform the development of new molecular-based spin qubits.

ACKNOWLEDGMENTS

We thank E. Williams and N. de Leon for useful conversations, K. Ellers for early work on the experiment, A. Anderson for assistance with use of the computing cluster, and J. Kubasek and B. Crepeau for significant technical assistance. This work was supported by the National Science Foundation under grant nos. DMR-1708692 and DMR-2207624. JRF acknowledges the support of the Amherst College Senior Sabbatical Fellowship Program, which is funded in part by the H. Axel Schupf '57 Fund for Intellectual Life. This work was performed in part using high-performance computing equipment at Amherst College obtained under National Science Foundation Grant No. 2117377. Any opinions, findings, and conclusions or recommendations expressed in this publication are those of the authors and do not necessarily reflect the views of the National Science Foundation.

- [1] M. Kjaergaard, M. E. Schwartz, J. Braumüller, P. Krantz, J. I.-J. Wang, S. Gustavsson, and W. D. Oliver, Superconducting Qubits: Current State of Play, *Annual Review of Condensed Matter Physics* **11**, 369 (2020).
- [2] C. D. Bruzewicz, J. Chiaverini, R. McConnell, and J. M. Sage, Trapped-Ion Quantum Computing: Progress and Challenges, *Applied Physics Reviews* **6**, 021314 (2019).
- [3] J. J. L. Morton, D. R. McCamey, M. A. Eriksson, and S. A. Lyon, Embracing the Quantum Limit in Silicon Computing, *Nature* **479**, 345 (2011).
- [4] A. J. Heinrich, W. D. Oliver, L. M. K. Vandersypen, A. Ardavan, R. Sessoli, D. Loss, A. B. Jayich, J. Fernandez-Rossier, A. Laucht, and A. Morello, Quantum-Coherent Nanoscience, *Nat. Nanotechnol.* **16**, 1318 (2021).
- [5] E. Coronado, Molecular Magnetism: From Chemical Design to Spin Control in Molecules, Materials and Devices, *Nat Rev Mater* **5**, 87 (2019).
- [6] A. Chiesa, S. Roca, S. Chicco, M. de Ory, A. Gómez-León, A. Gomez, D. Zueco, F. Luis, and S. Carretta, Blueprint for a Molecular-Spin Quantum Processor, *Physical Review Applied* **19**, 064060 (2023).
- [7] A. Gaita-Ariño, F. Luis, S. Hill, and E. Coronado, Molecular spins for quantum computation, *Nature Chemistry* **11**, 301 (2019).
- [8] J. H. Wesenberg, A. Ardavan, G. A. D. Briggs, J. J. L. Morton, R. J. Schoelkopf, D. I. Schuster, and K. Mølmer, Quantum Computing with an Electron Spin Ensemble, *Physical Review Letters* **103**, 070502 (2009).
- [9] J. R. Friedman and M. P. Sarachik, Single-Molecule Nanomagnets, *Annu. Rev. Condens. Matter Phys.* **1**, 109 (2010).
- [10] M. N. Leuenberger and D. Loss, Quantum Computing in Molecular Magnets, *Nature* **410**, 789 (2001).
- [11] J. Tejada, E. M. Chudnovsky, E. del Barco, J. M. Hernandez, and T. P. Spiller, Magnetic Qubits as Hardware for Quantum Computers, *Nanotechnology* **12**, 181 (2001).
- [12] F. Luis, F. L. Mettes, J. Tejada, D. Gatteschi, and L. J. De Jongh, Observation of Quantum Coherence in Mesoscopic Molecular Magnets, *Phys. Rev. Lett.* **85**, 4377 (2000).
- [13] A. Chiesa, P. Santini, E. Garlatti, F. Luis, and S. Carretta, Molecular Nanomagnets: A Viable Path toward Quantum Information Processing?, *Reports on Progress in Physics* **87**, 034501 (2024).
- [14] D. Vion, A. Aassime, A. Cottet, P. Joyez, H. Pothier, C. Urbina, D. Esteve, and M. H. Devoret, Manipulating the Quantum State of an Electrical Circuit, *Science* **296**, 886 (2002).
- [15] M. H. Devoret and R. J. Schoelkopf, Superconducting Circuits for Quantum Information: An Outlook, *Science* **339**, 1169 (2013).
- [16] P. Krantz, M. Kjaergaard, F. Yan, T. P. Orlando, S. Gustavsson, and W. D. Oliver, A quantum engineer's guide to superconducting qubits, *Applied Physics Reviews* **6**, 021318 (2019).
- [17] V. E. Manucharyan, J. Koch, L. I. Glazman, and M. H. Devoret, Fluxonium: Single Cooper-Pair Circuit Free of Charge Offsets, *Science* **326**, 113 (2009).
- [18] A. Somoroff, Q. Ficheux, R. A. Mencia, H. Xiong, R. Kuzmin, and V. E. Manucharyan, Millisecond Coherence in a Superconducting Qubit, *Physical Review Letters* **130**, 267001 (2023).
- [19] G. Wolfowicz, A. M. Tyryshkin, R. E. George, H. Riemann, N. V. Abrosimov, P. Becker, H.-J. Pohl, M. L. W. Thewalt, S. A. Lyon, and J. J. L. Morton, Atomic clock transitions in silicon-based spin qubits, *Nature Nanotechnology* **8**, 561 (2013).
- [20] M. Shiddiq, D. Komijani, Y. Duan, A. Gaita-Ariño, E. Coronado, and S. Hill, Enhancing Coherence in Molecular Spin Qubits via Atomic Clock Transitions, *Nature* **531**, 348 (2016).
- [21] C. Collett, K.-I. Ellers, N. Russo, K. Kittilstved, G. Timco, R. Winpenny, and J. Friedman, A Clock Transition in the CrMn Molecular Nanomagnet, *Magnetochemistry* **5**, 4 (2019).
- [22] K. Kundu, J. R. K. White, S. A. Moehring, J. M. Yu, J. W. Ziller, F. Furche, W. J. Evans, and S. Hill, A 9.2-GHz clock transition in a Lu(II) molecular spin qubit arising from a 3,467-MHz hyperfine interaction, *Nature Chemistry* **14**, 392 (2022).
- [23] J. M. Zadrozny, A. T. Gallagher, T. D. Harris, and D. E. Freedman, A Porous Array of Clock Qubits, *Journal of the American Chemical Society* **139**, 7089 (2017).
- [24] M. Rubín-Osanz, F. Lambert, F. Shao, E. Rivière, R. Guillot, N. Suaud, N. Guihéry, D. Zueco, A.-L. Barra, T. Mallah, and F. Luis, Chemical tuning of spin clock transitions in molecular monomers based on nuclear spin-free Ni(II), *Chemical Science* **12**, 5123 (2021).
- [25] M. Gakiya-Teruya, R. Stewart, L. Peng, S. Liu, C. Li, H.-P. Cheng, G. Chan, S. Hill, and M. Shatruk, A 54.6 GHz Clock Transition in Ho³⁺ Electron Spin Qubits Assembled into a Metal-Organic Framework (2025), preprint, DOI:10.26434/chemrxiv-2025-s62qg.
- [26] I. Tlemsani, F. Lambert, N. Suaud, C. Herrero, R. Guillot, A.-L. Barra, S. Gambarelli, and T. Mallah, Assessing the Robustness of the Clock Transition in a Mononuclear S = 1 Ni(II) Complex Spin Qubit, *Journal of the American Chemical Society* **147**, 4685 (2025).
- [27] S. Giménez-Santamarina, S. Cardona-Serra, J. M. Clemente-Juan, A. Gaita-Ariño, and E. Coronado, Exploiting clock transitions for the chemical design of resilient molecular spin qubits, *Chemical Science* **11**, 10718 (2020).
- [28] S. G. Lewis, K. E. Smyser, and J. D. Eaves, Clock transitions guard against spin decoherence in singlet fission, *The Journal of Chemical Physics* **155**, 194109 (2021).
- [29] B. C. Sheehan, G. Chen, and J. R. Friedman, Clock transitions generated by defects in silica glass, *Applied Physics Letters* **125**, 254003 (2024).
- [30] C. A. Collett, P. Santini, S. Carretta, and J. R. Friedman, Constructing Clock-Transition-Based Two-Qubit Gates from Dimers of Molecular Nanomagnets, *Phys. Rev. Research* **2**, 032037 (2020).
- [31] D. W. Laorenza, A. Kairalapova, S. L. Bayliss, T. Goldzak, S. M. Greene, L. R. Weiss, P. Deb, P. J. Mintun, K. A. Collins, D. D. Awschalom, T. C. Berkelbach, and D. E. Freedman, Tunable Cr⁴⁺ Molecular Color Centers, *Journal of the American Chemical Society* **143**, 21350 (2021).
- [32] S. L. Bayliss, P. Deb, D. W. Laorenza, M. Onizhuk,

- G. Galli, D. E. Freedman, and D. D. Awschalom, Enhancing Spin Coherence in Optically Addressable Molecular Qubits through Host-Matrix Control, *Phys. Rev. X* **12**, 031028 (2022).
- [33] J. J. Henderson, C. M. Ramsey, E. Del Barco, T. C. Stamatatos, and G. Christou, Control of the Inhomogeneity Degree by Magnetic Dilution in Crystals of Antiferromagnetic Molecular Rings, *Phys. Rev. B* **78**, 214413 (2008).
- [34] C. J. Wedge, G. A. Timco, E. T. Spielberg, R. E. George, F. Tuna, S. Rigby, E. J. L. McInnes, R. E. P. Winpenny, S. J. Blundell, and A. Ardavan, Chemical Engineering of Molecular Qubits, *Physical Review Letters* **108**, 107204 (2012).
- [35] S. Mondal and A. Lunghi, Spin-phonon decoherence in solid-state paramagnetic defects from first principles, *npj Computational Materials* **9**, 120 (2023).
- [36] F. Luis, M. J. Martínez-Pérez, O. Montero, E. Coronado, S. Cardona-Serra, C. Martí-Gastaldo, J. M. Clemente-Juan, J. Sesé, D. Drung, and T. Schurig, Spin-lattice relaxation via quantum tunneling in an $\{\text{Er}^{\text{III}}\}$ -polyoxometalate molecular magnet, *Physical Review B* **82**, 060403 (2010).
- [37] A. Ullah, J. Cerdá, J. J. Baldoví, S. A. Varganov, J. Aragó, and A. Gaita-Ariño, In Silico Molecular Engineering of Dysprosium-Based Complexes to Decouple Spin Energy Levels from Molecular Vibrations, *The Journal of Physical Chemistry Letters* **10**, 7678 (2019).
- [38] F. K. Larsen, E. J. L. McInnes, H. E. Mkami, J. Overgaard, S. Piligkos, G. Rajaraman, E. Rentschler, A. A. Smith, G. M. Smith, V. Boote, M. Jennings, G. A. Timco, and R. E. P. Winpenny, Synthesis and Characterization of Heterometallic $\{\text{Cr}_7\text{M}\}$ Wheels, *Angewandte Chemie International Edition* **42**, 101 (2003).
- [39] S. Piligkos, H. Weihe, E. Bill, F. Neese, H. El Mkami, G. M. Smith, D. Collison, G. Rajaraman, G. A. Timco, R. E. P. Winpenny, and E. J. L. McInnes, EPR Spectroscopy of a Family of $\text{Cr}^{\text{III}}\text{M}^{\text{II}}$ ($\text{M} = \text{Cd}, \text{Zn}, \text{Mn}, \text{Ni}$) “Wheels”: Studies of Isostructural Compounds with Different Spin Ground States, *Chemistry – A European Journal* **15**, 3152 (2009).
- [40] A. Ardavan, O. Rival, J. J. L. Morton, S. J. Blundell, A. M. Tyryshkin, G. A. Timco, and R. E. P. Winpenny, Will Spin-Relaxation Times in Molecular Magnets Permit Quantum Information Processing?, *Physical Review Letters* **98**, 057201 (2007).
- [41] G. A. Timco, S. Carretta, F. Troiani, F. Tuna, R. J. Pritchard, C. A. Muryn, E. J. L. McInnes, A. Ghirri, A. Candini, P. Santini, G. Amoretti, M. Affronte, and R. E. P. Winpenny, Engineering the Coupling between Molecular Spin Qubits by Coordination Chemistry, *Nature Nanotechnology* **4**, 173 (2009).
- [42] A. Ardavan, A. M. Bowen, A. Fernandez, A. J. Fielding, D. Kaminski, F. Moro, C. A. Muryn, M. D. Wise, A. Ruggi, E. J. L. McInnes, K. Severin, G. A. Timco, C. R. Timmel, F. Tuna, G. F. S. Whitehead, and R. E. P. Winpenny, Engineering Coherent Interactions in Molecular Nanomagnet Dimers, *npj Quantum Inf* **1**, 15012 (2015).
- [43] J. Liu, J. Mrozek, W. K. Myers, G. A. Timco, R. E. P. Winpenny, B. Kintzel, W. Plass, and A. Ardavan, Electric Field Control of Spins in Molecular Magnets, *Phys. Rev. Lett.* **122**, 037202 (2019).
- [44] A. Chiesa, G. F. S. Whitehead, S. Carretta, L. Carthy, G. A. Timco, S. J. Teat, G. Amoretti, E. Pavarini, R. E. P. Winpenny, and P. Santini, Molecular nanomagnets with switchable coupling for quantum simulation, *Scientific Reports* **4**, 7423 (2014).
- [45] J. Ferrando-Soria, E. Moreno Pineda, A. Chiesa, A. Fernandez, S. A. Magee, S. Carretta, P. Santini, I. J. Vitorica-Yrezabal, F. Tuna, G. A. Timco, E. J. L. McInnes, and R. E. P. Winpenny, A modular design of molecular qubits to implement universal quantum gates, *Nature Communications* **7**, 11377 (2016).
- [46] T. Lancaster, S. J. Blundell, F. L. Pratt, I. Franke, A. J. Steele, P. J. Baker, Z. Salman, C. Baines, I. Watanabe, S. Carretta, G. A. Timco, and R. E. P. Winpenny, Relaxation of muon spins in molecular nanomagnets, *Physical Review B* **81**, 140409 (2010).
- [47] K. Kundu, J. Chen, S. Hoffman, J. Marbey, D. Komijani, Y. Duan, A. Gaita-Ariño, J. Stanton, X. Zhang, H.-P. Cheng, and S. Hill, Electron-nuclear decoupling at a spin clock transition, *Communications Physics* **6**, 38 (2023).
- [48] D. X. Ngo, K. R. McClain, J. Hrubý, Y. J. Franzke, K. Kundu, H. Kwon, C. A. Gould, B. G. Harvey, S. Hill, and J. R. Long, Large Hyperfine Coupling Arising from Pseudo-2S Ground States in a Series of Lutetium(II) Metallocene Complexes, *Journal of the American Chemical Society* **147**, 13799 (2025).
- [49] See Supplemental Material at [URL will be inserted by publisher] for additional data and calculation details.
- [50] F. Moro, D. Kaminski, F. Tuna, G. F. S. Whitehead, G. A. Timco, D. Collison, R. E. P. Winpenny, A. Ardavan, and E. J. L. McInnes, Coherent electron spin manipulation in a dilute oriented ensemble of molecular nanomagnets: Pulsed EPR on doped single crystals, *Chem. Commun.* **50**, 91 (2014).
- [51] W. Froncisz and J. S. Hyde, The loop-gap resonator: A new microwave lumped circuit ESR sample structure, *Journal of Magnetic Resonance* (1969) **47**, 515 (1982).
- [52] G. Joshi, J. Kubasek, I. Nikolov, B. Sheehan, T. A. Costa, R. A. Allão Cassaro, and J. R. Friedman, Adjustable coupling and in situ variable frequency electron paramagnetic resonance probe with loop-gap resonators for spectroscopy up to X-band, *Review of Scientific Instruments* **91**, 023104 (2020).
- [53] M. J. Biercuk, A. C. Doherty, and H. Uys, Dynamical decoupling sequence construction as a filter-design problem, *Journal of Physics B: Atomic, Molecular and Optical Physics* **44**, 154002 (2011).
- [54] G. Jeschke and A. Schweiger, Hyperfine decoupling in electron spin resonance, *The Journal of Chemical Physics* **106**, 9979 (1997).
- [55] A. M. Souza, G. A. Álvarez, and D. Suter, Robust dynamical decoupling, *Philosophical Transactions of the Royal Society A: Mathematical, Physical and Engineering Sciences* **370**, 4748 (2012).
- [56] A. Schweiger and G. Jeschke, *Principles of Pulse Electron Paramagnetic Resonance* (Oxford University Press, Oxford, New York, 2001).
- [57] G. A. Álvarez and D. Suter, Measuring the Spectrum of Colored Noise by Dynamical Decoupling, *Phys. Rev. Lett.* **107**, 230501 (2011).
- [58] N. Bar-Gill, L. M. Pham, C. Belthangady, D. Le Sage, P. Cappellaro, J. R. Maze, M. D. Lukin, A. Yacoby, and R. Walsworth, Suppression of spin-bath dynamics for improved coherence of multi-spin-qubit systems, *Nature Communications* **3**, 858 (2012).
- [59] B. A. Myers, A. Ariyaratne, and A. C. B. Jayich, Double-

- Quantum Spin-Relaxation Limits to Coherence of Near-Surface Nitrogen-Vacancy Centers, *Phys. Rev. Lett.* **118**, 197201 (2017).
- [60] E. Q. Williams and C. Ramanathan, Characterizing the magnetic noise power spectrum of dark spins in diamond, *New Journal of Physics* **27**, 033007 (2025).
 - [61] J. Soetbeer, L. F. Ibáñez, Z. Berkson, Y. Polyhach, and G. Jeschke, Regularized Dynamical Decoupling Noise Spectroscopy – a Decoherence Descriptor for Radicals in Glassy Matrices, *Physical Chemistry Chemical Physics* **23**, 21664 (2021).
 - [62] Ł. Cywiński, R. M. Lutchyn, C. P. Nave, and S. Das Sarma, How to Enhance Dephasing Time in Superconducting Qubits, *Physical Review B* **77**, 174509 (2008).
 - [63] F. K. Malinowski, F. Martins, P. D. Nissen, E. Barnes, Ł. Cywiński, M. S. Rudner, S. Fallahi, G. C. Gardner, M. J. Manfra, C. M. Marcus, and F. Kuemmeth, Notch Filtering the Nuclear Environment of a Spin Qubit, *Nature Nanotechnology* **12**, 16 (2017).
 - [64] W. M. Witzel, K. Young, and S. Das Sarma, Converting a real quantum spin bath to an effective classical noise acting on a central spin, *Physical Review B* **90**, 115431 (2014).
 - [65] W.-L. Ma, G. Wolfowicz, S.-S. Li, J. J. L. Morton, and R.-B. Liu, Classical nature of nuclear spin noise near clock transitions of Bi donors in silicon, *Physical Review B* **92**, 161403 (2015).
 - [66] G.-L. Zhang, W.-L. Ma, and R.-B. Liu, Cluster correlation expansion for studying decoherence of clock transitions in spin baths, *Physical Review B* **102**, 245303 (2020).
 - [67] P. Schätzle, R. Ghassemizadeh, D. F. Urban, T. Wellens, P. Knittel, F. Reiter, J. Jeske, and W. Hahn, Spin coherence in strongly coupled spin baths in quasi-two-dimensional layers, *Physical Review B* **110**, L220302 (2024), arXiv:2401.16169 [quant-ph].
 - [68] M. Onizhuk, Y.-X. Wang, J. Nagura, A. A. Clerk, and G. Galli, Understanding Central Spin Decoherence Due to Interacting Dissipative Spin Baths, *Physical Review Letters* **132**, 250401 (2024).
 - [69] L. Ratini, G. Sansone, E. Garlatti, F. Petiziol, S. Carretta, and P. Santini, Mitigating decoherence in molecular spin qubits (2025), preprint, arXiv:2504.06057 [quant-ph].
 - [70] M. Joos, D. Bluvstein, Y. Lyu, D. Weld, and A. Bleszynski Jayich, Protecting qubit coherence by spectrally engineered driving of the spin environment, *npj Quantum Information* **8**, 47 (2022).
 - [71] M. Onizhuk and G. Galli, Colloquium: Decoherence of solid-state spin qubits: A computational perspective, *Reviews of Modern Physics* **97**, 021001 (2025).
 - [72] M. Onizhuk, K. C. Miao, J. P. Blanton, H. Ma, C. P. Anderson, A. Bourassa, D. D. Awschalom, and G. Galli, Probing the Coherence of Solid-State Qubits at Avoided Crossings, *PRX Quantum* **2**, 010311 (2021).
 - [73] R. Stewart, A. B. Canaj, S. Liu, E. Regincós Martí, A. Celmina, G. Nichol, H.-P. Cheng, M. Murrie, and S. Hill, Engineering Clock Transitions in Molecular Lanthanide Complexes, *Journal of the American Chemical Society* **146**, 11083 (2024).
 - [74] A. A. Clerk, K. W. Lehnert, P. Bertet, J. R. Petta, and Y. Nakamura, Hybrid Quantum Systems with Circuit Quantum Electrodynamics, *Nature Physics* **16**, 257 (2020).
 - [75] I. Gimeno, V. Rollano, D. Zueco, Y. Duan, M. C. de Ory, A. Gomez, A. Gaita-Ariño, C. Sánchez-Azqueta, T. Astner, D. Granados, S. Hill, J. Majer, E. Coronado, and F. Luis, Optimal Coupling of HoW₁₀ Molecular Magnets to Superconducting Circuits near Spin Clock Transitions, *Physical Review Applied* **20**, 044070 (2023).
 - [76] M. Jenkins, T. Hümmer, M. J. Martínez-Pérez, J. García-Ripoll, D. Zueco, and F. Luis, Coupling single-molecule magnets to quantum circuits, *New Journal of Physics* **15**, 095007 (2013).
 - [77] S. Carretta, D. Zueco, A. Chiesa, Á. Gómez-León, and F. Luis, A perspective on scaling up quantum computation with molecular spins, *Applied Physics Letters* **118**, 240501 (2021).

Supplementary Material for Enhancing Coherence with a Clock Transition and Dynamical Decoupling in the Cr₇Mn Molecular Nanomagnet

Guanchu Chen,^{1,2} Brendan C. Sheehan,^{1,2,*} Ilija Nikolov,^{1,†} James W. Logan,^{1,*}
Charles A. Collett,^{1,‡} Gajadhar Joshi,^{1,§} Grigore A. Timco,³ Jillian E. Denhardt,^{4,¶}
Kevin R. Kittilstved,^{4,**} Richard E. P. Winpenny,³ and Jonathan R. Friedman^{1,2,††}

¹*Department of Physics and Astronomy,
Amherst College, Amherst, MA 01002, USA*

²*Department of Physics, University of Massachusetts Amherst, Amherst, MA 01003, USA*

³*Department of Chemistry, The University of Manchester, Manchester M13 9PL, UK*

⁴*Department of Chemistry, University of Massachusetts, Amherst, MA 01003, USA*

(Dated: July 18, 2025)

I. INHOMOGENEOUS BROADENING

The inhomogeneous broadening can be seen in the broad response of ESR echo signal over a wide range of frequencies. As shown in Fig. S1, at zero field we see significant echo signal across a frequency range of ~ 2.5 GHz, with 3 different resonators – the frequency of each resonator is tuned over the range indicated by a single color through use of a dielectric. At zero field, the transitions frequency is determined exclusively by the transverse anisotropy: $\epsilon = 2E$; thus, the observations provide a direct indication of the inhomogeneity in E . It is worth noting that we have seen echo beyond this range; the data shown is from a particular

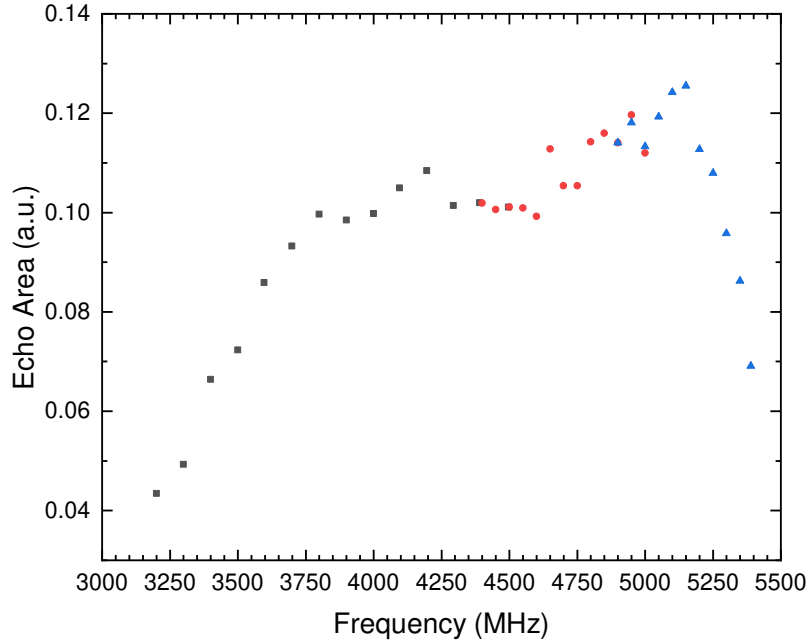


FIG. S1. Zero-field frequency response of **2** at the clock transition. The data is from 1% toluene solution sample at 1.8 K with three different resonators (marked with colors), indicating a very broad frequency response. Since this is a zero-field signal, we can infer a broad inhomogeneity in the anisotropy parameter E .

* Current address: Department of Physics and Astronomy, Dartmouth College, Hanover, NH 03755, USA

† Current address: Department of Physics, Brown University, Providence, RI 02912, USA

‡ Current address: Department of Physics, Hamilton College, Clinton, NY 13323, USA

§ Current address: Center for Integrated Nanotechnologies, Sandia National Laboratories, Albuquerque, NM 87123, USA

¶ Current address: University of Hawai'i at Mānoa, Honolulu, HI 96822, USA

** Current address: Department of Chemistry, Washington State University, Pullman, 99164-4630, USA

†† jrfriedman@amherst.edu

experiment with controlled frequency response.

II. HOLE BURNING

Despite the broad inhomogeneity, at any given drive frequency, we are only exciting a small sub-ensemble of the spins. This is demonstrated with a hole-burning experiment, illustrated in Fig. S2(a). The sequence contains three pulses: a hole-burning pulse is followed after a time τ' by a traditional Hahn echo sequence ($\pi/2$ - τ - π - τ -echo), where τ is the delay time between Hahn pulses. The hole-burning pulse is detuned from the working ESR frequency by some detuning frequency Δf , which becomes the independent variable of the experiment. The hole-burning pulse has a duration of 2 μ s so that its linewidth is small compared to those of Hahn sequence pulses. The amplitude of the hole-burning pulse is kept small to prevent possible saturation effects. By sweeping Δf a hole is measured (an example is shown in Fig. S2(b)) and fit with a Voigt function. By changing time τ' , we are able to map the energy diffusion over time. From Fig. S2(c), we see that the full width at half maximum of the hole changes from ~ 1.5 MHz to ~ 2 MHz over 50 μ s of evolution. Our typical pulsed experiments were done within the time scale of tens of microseconds, meaning we only probed the resonant sub-ensemble of the system, before any significant spectral diffusion had occurred.

III. COMPARISON OF SAMPLE VARIANTS, DILUTIONS AND COOLING TECHNIQUES

Fig. S3 shows a comparison of echo signals from different Cr₇Mn sample variants, dilutions and cooling techniques. While signal strength naturally varies – largely due to concentration and also due to variations in the measurement circuit and other experimental conditions – we expect the coherence time T_2 to be more governed by intrinsic physical properties, and to exhibit more consistent and interpretable trends. The figure compares T_2 values for several samples, measured at a variety of frequencies. The most naive expectation is that T_2 should be enhanced by further dilution. However, we see very little change as concentration varies between 0.1% and 10%. When using the CPMG sequence – Fig. S4 – we do see some hint of a dependence of T_2 on concentration, but it is hard to draw strong conclusions from the

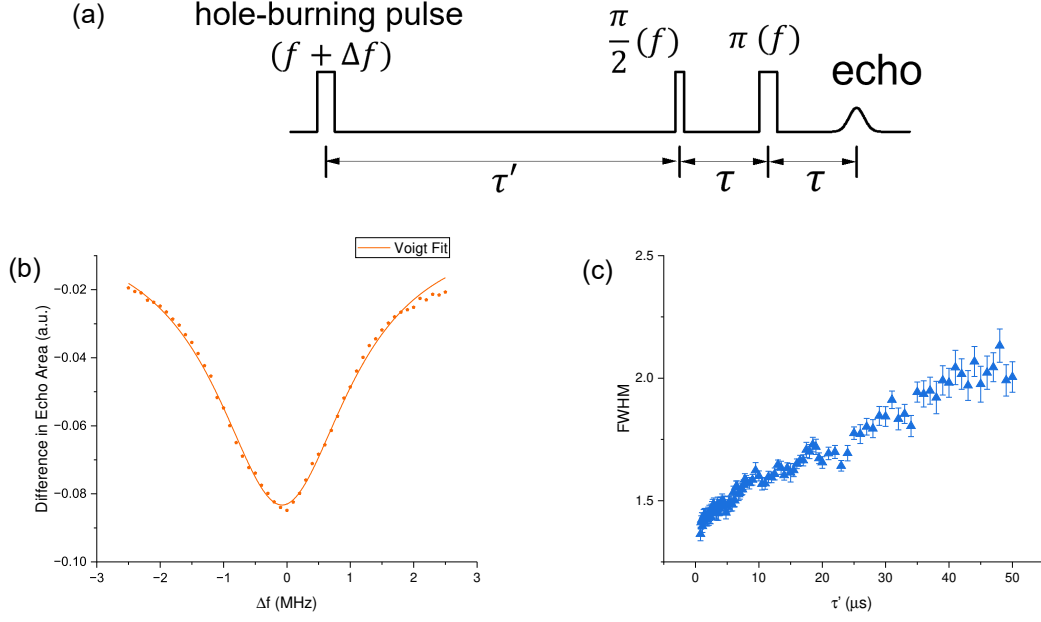


FIG. S2. Hole Burning Experiment. a) Pulse diagram of the hole-burning sequence. A delay of τ' follows the hole-burning pulse after which echo is detected with a Hahn sequence. b) Example of a burned hole. The hole-burning pulse is “soft”, having a long width of 2 μs . Data is measured with 10% dilution **2** toluene solution at 1.8 K and 5625 MHz. c) Evolution of FWHM of the burned hole. The diffusion happens slowly compared to the typical timescale of our pulsed experiments, i.e. T_2 : after 50 μs , the hole width increases from ~ 1.5 MHz to ~ 2 MHz.

data.

The measured T_2 value also does not seem to depend significantly on the solvent: liquid solutions using toluene or deuterated toluene solvents were studied as well as solid solutions by co-crystallizing Cr_7Mn with Ga_7Zn ; all show rather similar behavior. Variation of cation (comparing **1** with **2**) was also not found to have significant effect on the coherence. This indicates that the most pronounced noise contributing to T_2 originates from within the molecule itself.

IV. NOISE SPECTRUM CONVERSION COEFFICIENTS

We derive the conversion coefficients from the noise on \mathbf{B} to noise on ϵ by solving the Hamiltonian and then expanding it around the external field \mathbf{B}_0 . In Einstein notation,

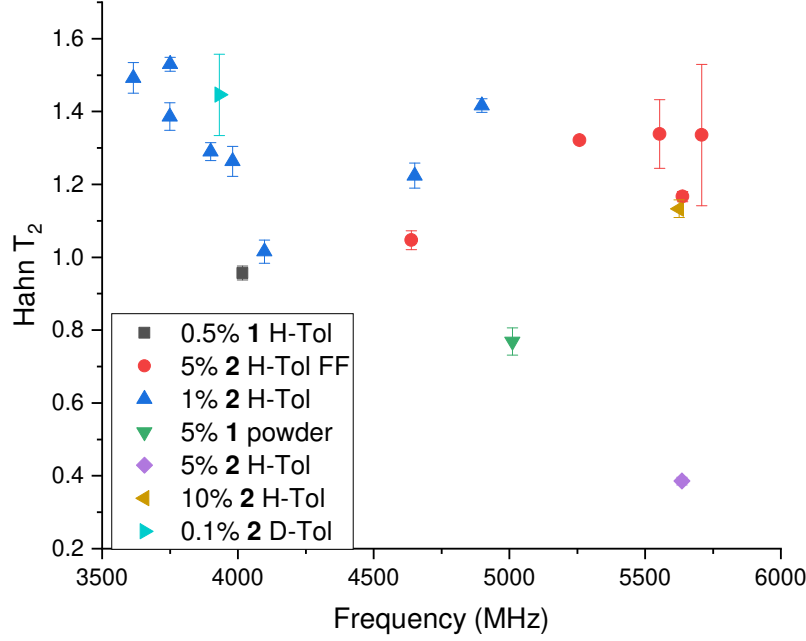


FIG. S3. Frequency dependency of Hahn T_2 at the zero-field clock transition from different sample variants, dilutions, solvent and cooling techniques. D-Tol indicates deuterated toluene, FF indicates a sample that was flash frozen, and powder refers to a solid solution sample of Cr_7Mn in Ga_7Zn .

denoting $\epsilon_i \equiv \frac{\partial \epsilon}{\partial B^i}$ and $\epsilon_{ij} \equiv \frac{\partial^2 \epsilon}{\partial B^i \partial B^j}$, a Taylor series expansion yields

$$\epsilon = \epsilon_0 + \underbrace{B^i \epsilon_i}_{2nd} + \underbrace{B^i B^j \epsilon_{ij}}_{3rd} + \underbrace{\frac{\partial \epsilon}{\partial E} \delta E}_{4th}, \quad (\text{S1})$$

where $B^i \equiv \int r^2 dr d\Omega b^i(\mathbf{r})$ is the collective induced field of the proton bath at the origin (location of the electronic spin), and δE is the dynamical deviation of anisotropy parameter E . The field $b^i(\mathbf{r})$ is defined below, cf. Eq. S10. It is easy to see there is no cross-correlation between terms (i.e., 2nd, 3rd, and 4th terms). Thus, to get the temporal autocorrelation of $\delta\epsilon = \epsilon - \text{E}[\epsilon]$, one can calculate the contribution of each term separately. For the second term in Eq. S1, we can get the contribution to $\text{E}[\delta\epsilon(t_1)\delta\epsilon(t_2)]$:

$$\text{corr}_2 \equiv \text{E}[\delta\epsilon(t_1)\delta\epsilon(t_2)] = \epsilon_i \epsilon_j \text{E}[B^i(t_1)B^j(t_2)]. \quad (\text{S2})$$

We assume the field coming from protons at different locations is uncorrelated, so

$$\text{E}[B^i(t_1)B^j(t_2)] = \int r^2 dr d\Omega \text{E}[b^i(\mathbf{r}, t_1)b^j(\mathbf{r}, t_2)] \quad (\text{S3})$$

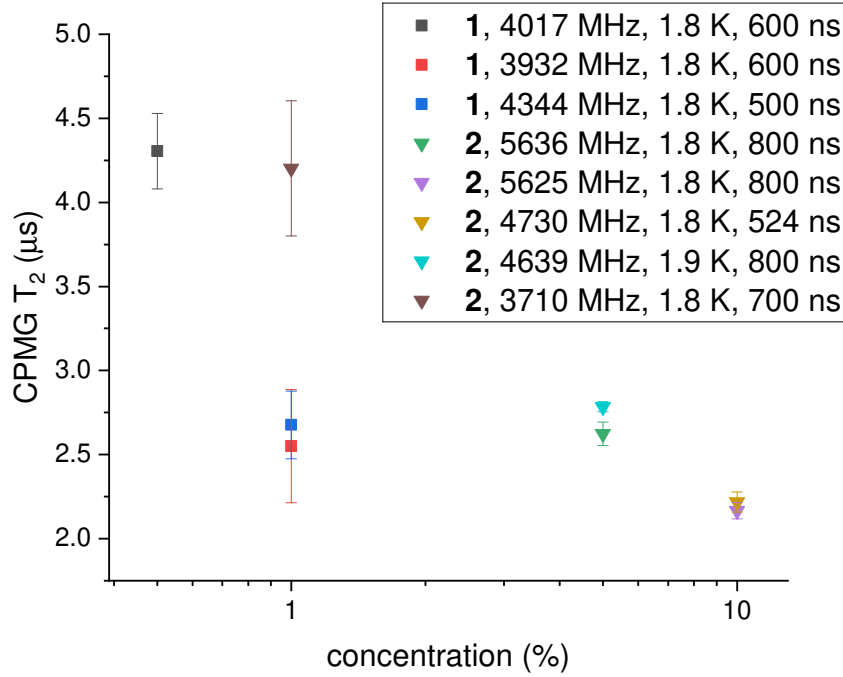


FIG. S4. CPMG T_2 dependence on dilution. The data is from various samples, as noted in legend, with frequencies, temperature, and τ of the CPMG sequences. The data appear to indicate longer T_2 with lower dilution, but the scatter makes it hard to infer strong conclusions.

As shown in the next section, $E[b^i(\mathbf{r}, t_1)b^j(\mathbf{r}, t_2)] = R_2(r)g^{i,j}(\theta, \phi) \cos(\omega_{L,0}T) \exp(-\frac{1}{2}\sigma T)$ with $T \equiv t_2 - t_1$, given our assumption that the noise arises from Larmor precession at frequency $\omega_{L,0}$. Then

$$\text{corr}_2 = \cos(\omega_{L,0}T)e^{-\frac{1}{2}\sigma T} \int R_2(r)r^2 dr \int d\Omega g^{i,j}(\theta, \phi) \epsilon_i \epsilon_j \quad (\text{S4})$$

$$\equiv \alpha C_1 \cos(\omega_{L,0}T)e^{-\frac{1}{2}\sigma T}, \quad (\text{S5})$$

defining $\alpha \equiv \int R_2(r)r^2 dr$ a fitting parameter reflecting the radial distribution in protons, and $C_1 \equiv \epsilon_i \epsilon_j \int d\Omega g^{i,j}(\theta, \phi)$, which can be calculated assuming an isotropic distribution of protons.

The same process can be carried out for the 3rd and 4th terms to obtain

$$\text{corr}_3 = \cos(2\omega_{L,0}T)e^{-2\sigma T} \int R_4(r)r^2 dr \int d\Omega g_2^{ijkl}(\theta, \phi) \epsilon_{ij} \epsilon_{kl} \quad (\text{S6})$$

$$\equiv \beta C_2 \cos(2\omega_{L,0}T)e^{-2\sigma T}, \quad (\text{S7})$$

$$\text{corr}_4 = \left(\frac{\partial \epsilon}{\partial E} \right)^2 \text{E}[\delta E(t_1) \delta E(t_2)] \quad (\text{S8})$$

$$\equiv C_3 \text{E}[\delta E(t_1) \delta E(t_2)], \quad (\text{S9})$$

in which $\beta \equiv \int R_4(r)r^2 dr$, $C_2 \equiv \epsilon_{ij} \epsilon_{kl} \int d\Omega g_2^{ijkl}(\theta, \phi)$, $C_3 \equiv \left(\frac{\partial \epsilon}{\partial E} \right)^2$, $\text{E}[\delta E(t_1) \delta E(t_2)] = \int \frac{d\omega}{2\pi} e^{-i\omega t} \gamma \cdot \frac{1}{\omega}$, following the *ad hoc* assumption of a $1/f$ spectrum for the noise in E .

V. NOISE ON LARMOR FREQUENCY

We treat each nuclear spin classically, as a magnetic dipole moment $\boldsymbol{\mu}$ at position \mathbf{r} . The induced magnetic field at the electronic spin located at the origin is

$$b^i(\mathbf{r}) = \frac{\mu_0 \mu}{4\pi r^3} (3\hat{r}^i \hat{r}_m \hat{\mu}^m - \hat{\mu}^i) \quad (\text{S10})$$

$$= \frac{\mu_0 \mu}{4\pi r^3} (3\hat{r}^i \hat{r}_m - \delta_m^i) \hat{\mu}^m \quad (\text{S11})$$

Then, for corr_2 , one obtains

$$\text{E}[b^i(\mathbf{r}, t_1) b^j(\mathbf{r}, t_2)] = R_2(r) (3\hat{r}^i \hat{r}_m - \delta_m^i) (3\hat{r}^j \hat{r}_n - \delta_n^j) \text{E}[\hat{\mu}^m(t_1) \hat{\mu}^n(t_2)] \quad (\text{S12})$$

$$\equiv R_2(r) \Theta_{mn}^{ij}(\theta, \phi) \text{E}[\hat{\mu}^m(t_1) \hat{\mu}^n(t_2)], \quad (\text{S13})$$

where $R_2(r) = \left(\frac{\mu_0 \mu}{4\pi r^3} \right)^2$ and $\Theta_{mn}^{ij}(\theta, \phi) = (3\hat{r}^i \hat{r}_m - \delta_m^i) (3\hat{r}^j \hat{r}_n - \delta_n^j)$. Similarly, for corr_3 , one finds

$$\text{E}[b^i(\mathbf{r}, t_1) b^j(\mathbf{r}, t_1) b^k(\mathbf{r}, t_2) b^l(\mathbf{r}, t_2)] = R_4(r) \Theta_{mnpq}^{ijkl}(\theta, \phi) \text{E}[\hat{\mu}^m(t_1) \hat{\mu}^n(t_1) \hat{\mu}^p(t_2) \hat{\mu}^q(t_2)] \quad (\text{S14})$$

For convenience, we define a new frame (XYZ) with the precession axis as the Z-axis so

$$\hat{\mu}_X = \hat{\mu}_\perp \cos\left(\int dt \omega_L + \varphi\right) \quad (\text{S15})$$

$$\hat{\mu}_Y = \hat{\mu}_\perp \sin\left(\int dt \omega_L + \varphi\right) \quad (\text{S16})$$

$$\hat{\mu}_Z = \hat{\mu}_\parallel \quad (\text{S17})$$

in which $\hat{\mu}_\perp$, $\hat{\mu}_\parallel$, and φ define the initial state at $t = 0$, which is assumed random, and $\omega_L = \omega_{L,0} + \delta\omega_L$. To illustrate how we get the damping cosine function in Eq. S4 and Eq. S6, we show how we calculate $E[\hat{\mu}_X(t_1)\hat{\mu}_X(t_2)]$:

$$E[\hat{\mu}_X(t_1)\hat{\mu}_X(t_2)] = E[\hat{\mu}_\perp^2 \cos(\int_0^{t_1} dt\omega_L + \varphi) \cos(\int_0^{t_2} dt\omega_L + \varphi)] \quad (\text{S18})$$

$$= \frac{1}{3} E[\exp \left[i \left(\omega_{L,0}(t_2 - t_1) + \int_{t_1}^{t_2} dt\delta\omega_L(t) \right) \right] + H.C.] \quad (\text{S19})$$

$$= \frac{2}{3} \cos(\omega_0 T) \exp \left[-\frac{1}{2}\sigma T \right], \quad (\text{S20})$$

obtained by first averaging over initial states (Eq. S19) ($\int \hat{\mu}_\perp^2 \sin\vartheta d\vartheta = \frac{4}{3}$, $\int \exp(2i\varphi) d\varphi = 0$) and then the noise in ω_L (Eq. S20), in which $\int_{t_1}^{t_2} dt\delta\omega_L(t)$ has a Gaussian distribution of $N(0, \sqrt{\sigma T})$. A similar calculation can be carried out for other terms and all terms in the new frame can be converted back to the molecule frame with a rotation matrix. All together, we can get $E[\hat{\mu}^m(t_1)\hat{\mu}^n(t_2)] = G^{mn} \cos(\omega_0 T) \exp[-\frac{1}{2}\sigma T]$, where G^{mn} is a matrix of constants reflecting the symmetry of our system. Plugging this back to Eq. S13, we get $g^{i,j}(\theta, \phi) \equiv \Theta_{mn}^{ij}(\theta, \phi) G^{mn}$. Similarly, for corr_3 , $E[\hat{\mu}^m(t_1)\hat{\mu}^n(t_1)\hat{\mu}^p(t_2)\hat{\mu}^q(t_2)] = 2G^{mnpq} E[\exp \left[i \left(2\omega_{L,0}(t_2 - t_1) + 2 \int_{t_1}^{t_2} dt\delta\omega_L(t) \right) \right] + H.C.] = G^{mnpq} \cos(2\omega_{L,0} T) \exp[-2\sigma T]$.

VI. ADDITIONAL DATA/SIMULATIONS

Fig. S5–S8 show the data at other field not shown in the main text but used in the fitting.

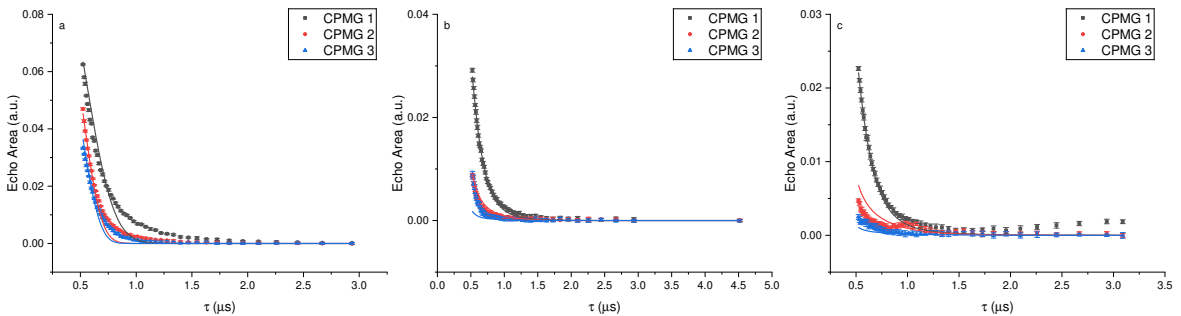


FIG. S5. Additional CPMG data (points) and fits (solid lines) at fields of (a) 25, (b) 50, and (c) 75 Oe.

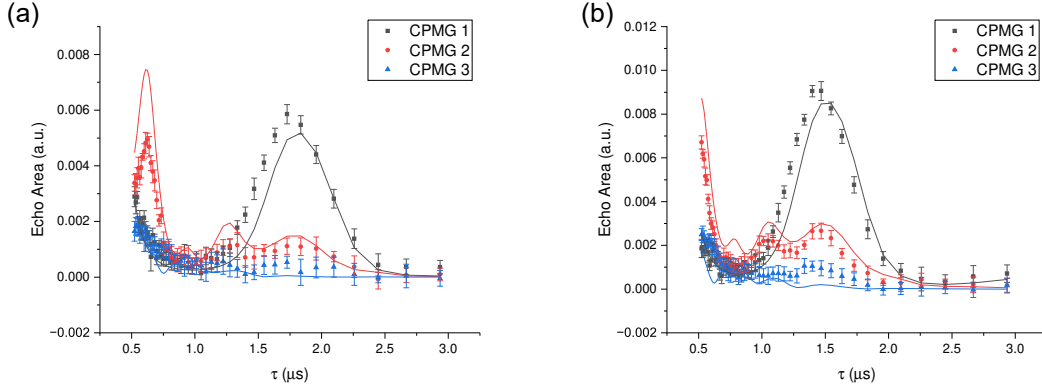


FIG. S6. Additional CPMG data (points) and fits (solid lines) at fields of (a) 125 and (b) 150 Oe.

VII. FITTING WITHOUT NOISE IN E

As presented in the main text, our noise/decoherence model includes field noise due to a nuclear spin bath as well as noise in the anisotropy parameter E , $S_E \propto 1/f$. This noise in E presents a limiting factor on decoherence at the CT, where the effects of field fluctuations are largely filtered out. At zero field, where the CT occurs, the only noise sources in our model that can lead to decoherence are $S_{B_I \otimes B_I}$ and S_E since S_{B_I} is filtered completely by the CT. This raises the question of whether the second-order field fluctuations $S_{B_I \otimes B_I}$ could be sufficient to account for our observed decoherence at zero field. Re-running a fit of our model at zero field, forcing $S_E = 0$ while allowing all other parameters to vary [1], produces the results shown in Fig. S9. The fit is far worse than what we obtain by including S_E , as shown in Fig. 10(a) in the main text. This strongly suggests that the fluctuations in E play an essential role in decoherence at the CT and that second-order fluctuations are insufficient to account for the observed zero-field behavior.

VIII. DISCUSSION OF COHERENT MODEL ON INTERMEDIATE RANGE OF FIELD

For intermediate-range fields, there is a revival of the signal after the system has seemingly fully decohered. Fig. S10 show the Hahn echo area in the range of 50–95 Oe. This revival is in fact consistent with ESEEM oscillations. The echo area initially decays in a quasi-exponential way, but then recovers at later times, producing a signal that peaks at a time

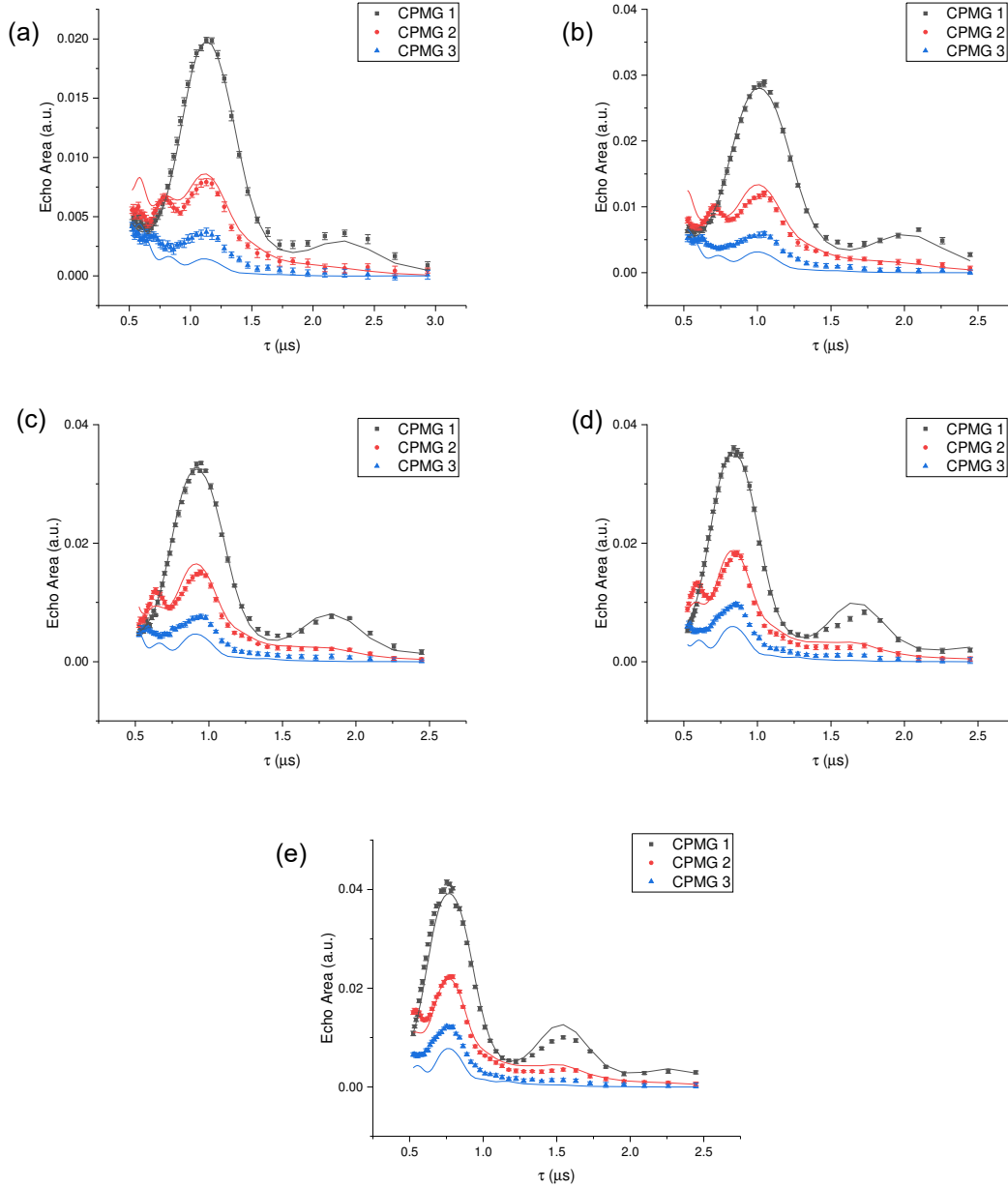


FIG. S7. Additional CPMG data (points) and fits (solid lines) at fields of (a) 200, (b) 225, (c) 250, (d) 275, and (e) 300 Oe.

that is roughly consistent with the Larmor precession frequency. We find that this behavior is not well produced with our coherent-model simulations, highlighting the advantage of modeling the environment as a noise source. Figure S11 illustrates the inability of the coherent-coupling model to adequately reproduce the data in this range of fields. In the top six panels (a-f), we show experimental and simulated results for a sampling of six fields in

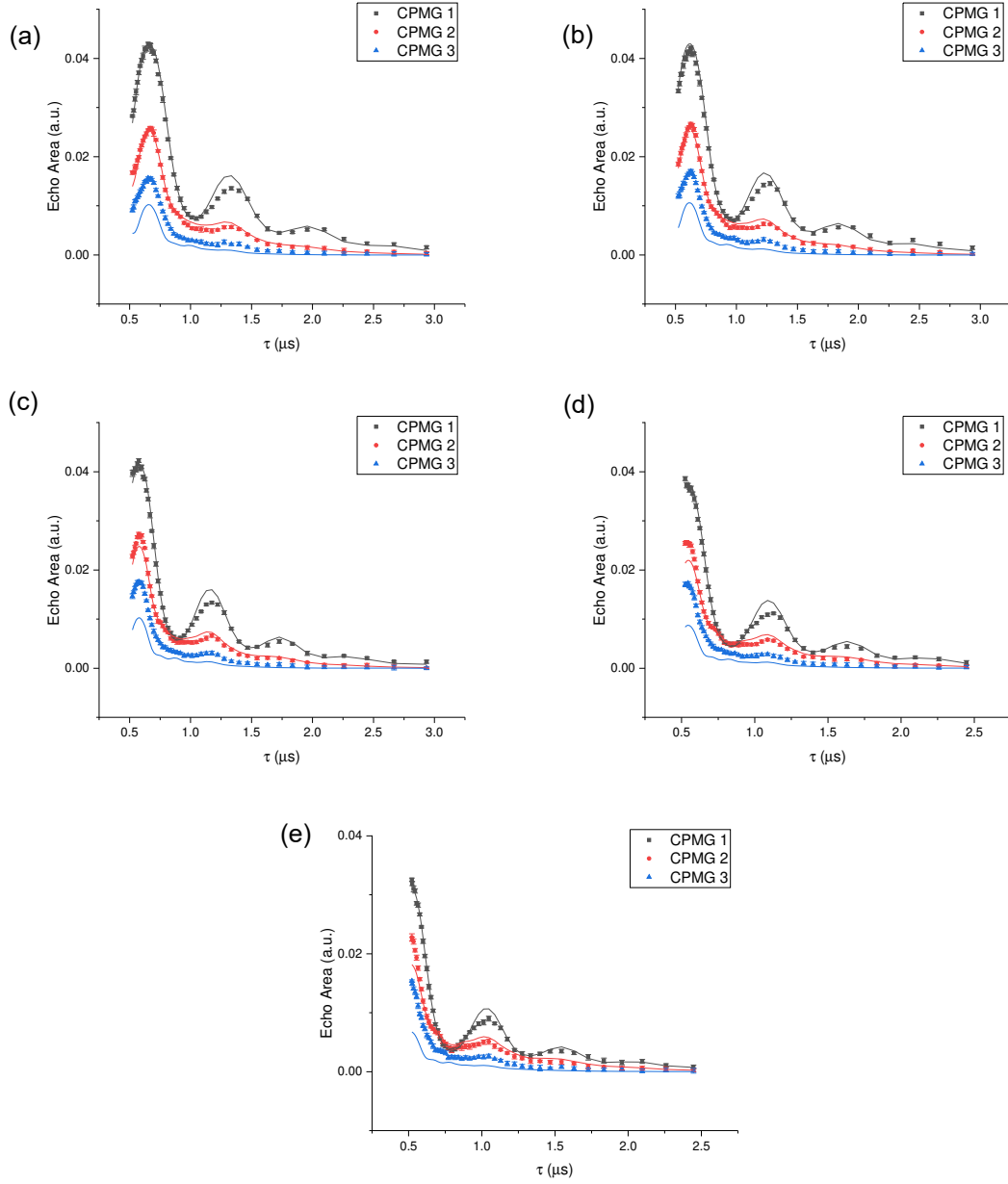


FIG. S8. Additional CPMG data (points) and fits (solid lines) at fields of (a) 350, (b) 375, (c) 400, (d) 425, and (e) 450 Oe.

this regime. The dashed lines represent the results of simulations without decoherence while the solid lines show the results of fitting. For the fitting, we fixed the hyperfine parameters to those found from the fitting of data in the 195 – 395 Oe field range and then refit the data over all fields, allowing all other parameters (T_2 for each field, scaling parameter, offset) to vary. There are two important failures of the simulations here: 1) Without decoherence,

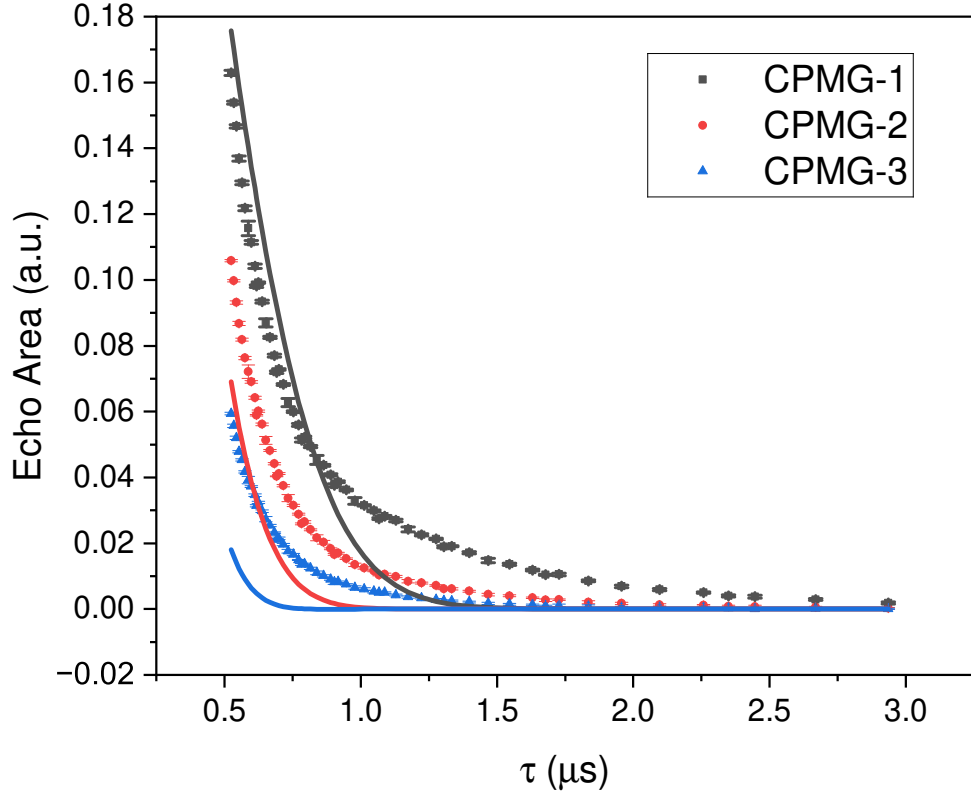


FIG. S9. The result of fitting the zero-field data after forcing $S_E = 0$. The fit is substantially worse in comparison to when S_E is included in the model, cf. Fig. 10(a) in the main text.

the simulations show a peak at values of 2τ (e.g. $\sim 3 \mu\text{s}$ for 75 Oe) where no peak is observed in the data. This peak corresponds to oscillations at about twice the Larmor frequency, a known effect in ESEEM. 2) The fitting is unable to meaningfully reproduce the data. One important observation is that the signal size in this range of fields is approximately an order of magnitude smaller than in the higher-field range. In order to account for the small signal size as well as the rapid decay of low values of τ and the absence of the low- τ peak, the fit yields an extremely fast decay that does not account for the signal revival at longer values of τ . Attempts to force T_2 to be larger to allow for observation of the revival results in a signal amplitude that is vastly larger than the observations in this regime.

To attempt to address the issues described above, we chose to reduce the hyperfine coupling strength by more than an order of magnitude: $A_{zz} = 0.2 \text{ MHz}$ and $A_{z\perp} = 0$. The motivation for doing this is to eliminate the low- τ peak in the simulations. An additional consequence of reducing A_{zz} to this small value makes the amplitude of the ESEEM oscilla-

tions much smaller than the observations. To compensate for this, we allowed for coupling of the electronic spin to a large number of protons, not just one as in our previous model. In other words, we update Eq. 2 (main text) to

$$\mathcal{H} = -DS_z^2 + E(S_x^2 - S_y^2) + g_s\mu_B\mathbf{B} \cdot \mathbf{S} + \sum_i (A_{zz}S_zI_{i,z} - g_p\mu_p\mathbf{B} \cdot \mathbf{I}_i). \quad (\text{S21})$$

For the small value of A_{zz} we use, we find that the ESEEM oscillations retain their shape as we increase the number of protons n_p in the sum and the oscillation amplitude scales linearly with n_p , which we treat as an additional fitting parameter. Figure S11(g-l) show the results of an attempt to employ this model. We indeed see that the additional low- τ peak is no longer visible in the damping-free simulations. However, the fit still fails to adequately reproduce the experimental data, again showing a short T_2 to account for the initial fast decay of the signal. Again, the fundamental issue here appears to be that longer values of T_2 , while allowing the simulations to exhibit oscillations, produce signal sizes that are much too large to match the experimental data.

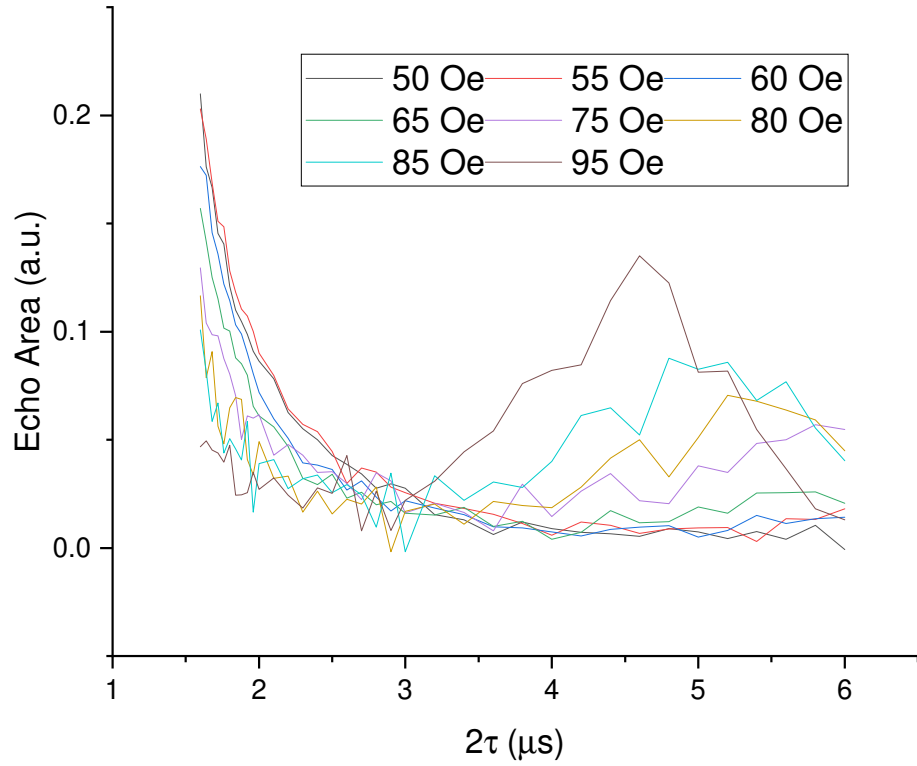


FIG. S10. Hahn echo area at intermediate fields, 50 – 95 Oe. The signal appears to revive after seemingly fully decohering. Data was taken with 5% dilution **2** toluene solution at 1.9 K and 4639 MHz.

[1] Excluding S_{B_I} since the simulations have no dependence on it at zero field.

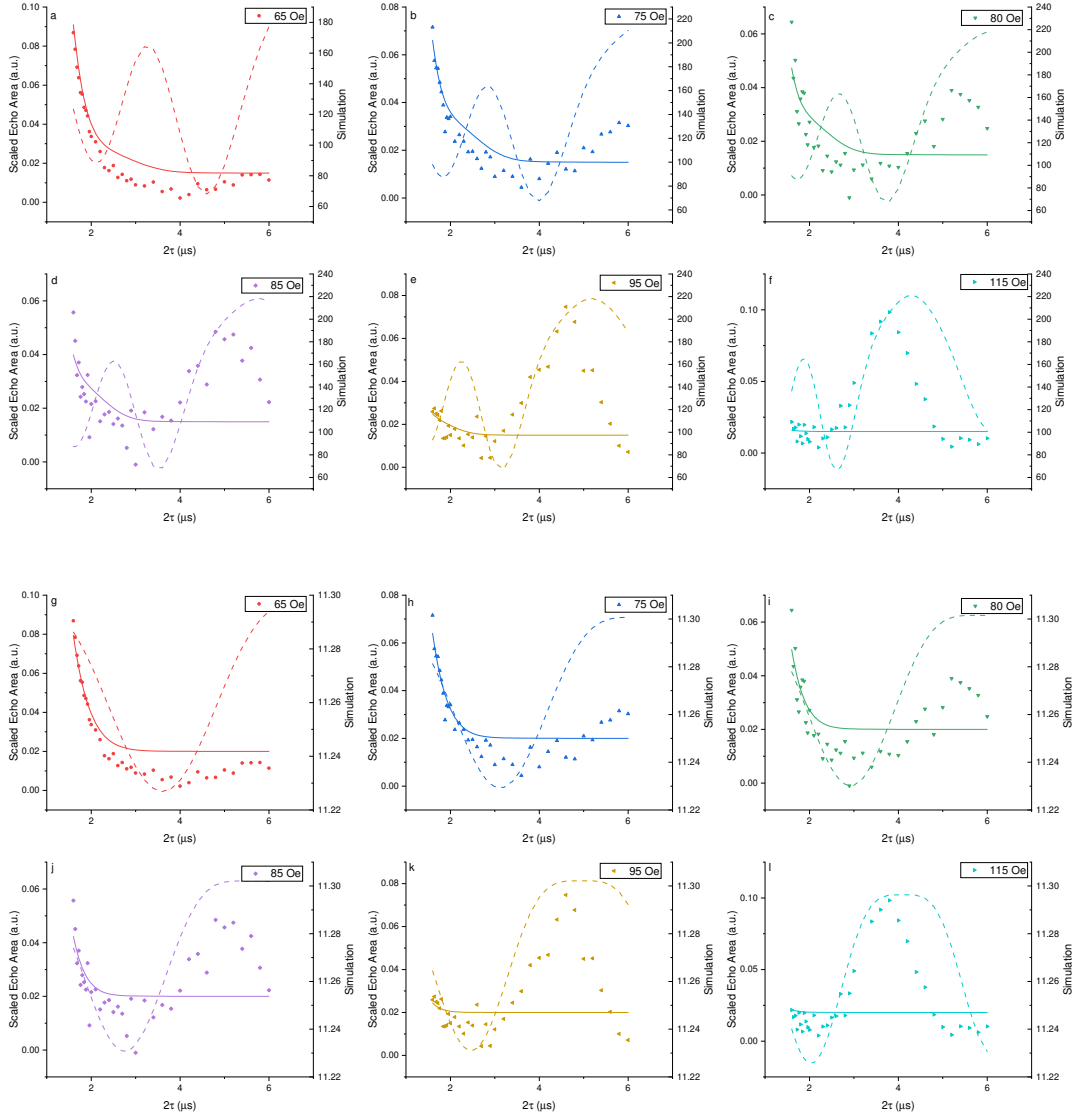


FIG. S11. Attempted fitting at intermediate field values with hyperfine coupling. Panels a–f show the results from the same procedure used for Fig. 9, as described in main text, except allowing for refitting the global scaling parameter and offset. Note that with these hyperfine coupling parameters, the undecohered waveform (dashed line) shows additional structure with small τ not present in the data. Panels g–l are the results from fitting using a model of coupling to multiple (n_p) protons with small values of hyperfine coupling, Eq. S21. The modulation frequency is largely the nuclear Larmor frequency as a result.